Secondary neutrons around clinical electron and proton beams

Georges Al Makdessi, PhD

Medical Physics Unit

McGill University, Montreal

A thesis submitted to McGill University in partial fulfillment of the requirements of the degree of Master of Science in Medical Radiation Physics

December 2017

Acknowledgements

In the first place, I would like to express my great appreciation to my thesis director, Professor John Kildea. Thank you for your support and guidance, for your efforts, your confidence in me and for your human and professional qualities.

I am very grateful for all the instructors and clinical staff for everything they taught me in my courses or during our precious discussions. Particularly, I would like to express special thanks to Dr Jan Seuntjens and Mr William Parker for their continual support.

I would like to offer my sincere gratitude to the Canadian Nuclear Safety Commission for its contribution to this work by supporting me financially. Special thanks to Dr Angel Licea for his help and support.

I would like to thank everyone who contributed to this work specially Robert Maglieri, Logan Montgomery and Jacques Dubeau.

I like to express my thankfulness to my family, my parents, my two brothers and my sister, who have continually encouraged and supported me while being proud of me. I thank God for having you.

Finally, I would like to express my deep appreciation to my wife Carole for all she has done for me during my Masters program. Thank you, Carole, for your assistance, your love and your sacrifices, and for helping me in finding hope, joy and enthusiasm in my most difficult moments. Thanks to my little Michel and my little Clara who, unknowingly, have contributed to this work through their joyful presence, sincerity and unconditional love.

Abstract

As is the case for high-energy photon beam therapy (> 10 MV), secondary neutrons are produced during electron and proton therapy. These neutrons, which extend in energy up to the maximum energy of the primary beam, result in a whole-body radiation dose to the patient that presents a risk for a second, radiation-induced, cancer. To account for the second-cancer risk, it is necessary to understand the spectra of the neutrons involved.

In this research project, the spectra of secondary neutrons arising from clinical electron and proton beams were measured. The neutron spectra around electron beams were measured for a Varian linear accelerator with maximum electron energy of 20 MeV. The neutron spectra around proton beams were measured in a treatment room with a gantry and a dedicated nozzle at the Skandion proton therapy clinic in Uppsala, Sweden. The proton beams were generated by the compact IBA Proteus Plus cyclotron, which has a maximum proton energy of 230 MeV.

Measurements were performed using the Nested Neutron Spectrometer (NNS™, Detec Inc, Gatineau Quebec). The NNS™ comprises a central He-3 detector (active neutron detection) with seven high density polyethylene shells that may be arranged around the detector in Russian doll fashion. The neutron spectra arising from proton beams were measured using a modified version of the NNS™ incorporating a brass moderator shell to provide an extended energy range (EER) for the detection of high-energy neutrons. The raw neutron data were unfolded using the Maximum a Posteriori (MAP) method (custom-written in C++) and the vendor-supplied moderator response functions for the NNS™. Note that the MAP is a modified version of the Maximum Likelihood Estimation Method (MLEM) that penalizes any high noise component. To plot the secondary neutron fluence as a function of energy, the ROOT data analysis library from

CERN was used. Additionally, the ICRP conversion coefficients were used to calculate the neutron ambient dose equivalent rates around the electron and proton beams.

The effect of several parameters on the neutron fluence rate and on the neutron dose equivalent rate were studied for each primary beam situation.

For the electron beams, it was observed that as the energy of the primary electron beam increases, the neutron fluence rate and dose equivalent rate increase. In addition, the presence of a solid water phantom in the primary electron beam does not affect the neutron spectra. However, when closing the jaws in the treatment head, the neutron fluence rate and dose equivalent rate increase significantly which means that the main production of secondary neutrons around electron beams lies in the treatment head of the linear accelerator.

For the proton beams, it was observed that as the energy of the primary proton beam increases, the neutron fluence rate and dose equivalent rate increase. The presence of a water phantom in the primary beam significantly enhances the direct and evaporation peaks of the neutron spectra which indicates that an important production of secondary neutrons around proton beams happens in the patient body. The evaporation and direct peaks of the neutron spectrum dominate the thermal peak when measuring on the couch (close to the neutron source), while the thermal peak dominates when measuring in the maze-room junction (far from the neutron source).

Keywords: secondary neutrons, electrons, protons, MLEM, MAP, neutron fluence rate, dose equivalent rate.

Résumé

Des neutrons secondaires sont produits pendant la thérapie par des faisceaux d'électrons et de protons, comme dans la thérapie par des photons à haute énergie (> 10 MV). Ces neutrons, qui s'étendent en énergie jusqu'à l'énergie maximale du faisceau primaire, entraînent une dose de radiation au corps entier du patient présentant un risque pour un second cancer induit par radiation. Pour tenir compte du deuxième risque de cancer, il est nécessaire de comprendre les spectres des neutrons impliqués.

Dans ce projet de recherche, on a mesuré les spectres des neutrons secondaires issus des faisceaux cliniques d'électrons et de protons. Les spectres de neutrons autour des faisceaux d'électrons ont été mesurés autour d'un accélérateur linéaire Varian avec une énergie électronique maximale de 20 MeV. Les spectres de neutrons autour des faisceaux de protons ont été mesurés dans une salle de traitement à la clinique Skandion à Uppsala, en Suède. Les faisceaux de protons ont été générés par le cyclotron compact IBA Proteus Plus, ayant une énergie maximale de protons égale à 230 MeV.

Les mesures ont été réalisées à l'aide du Spectromètre Nested Neutron Spectrometer (NNS™, Detec Inc, Gatineau Québec). Le NNS™ comprend un détecteur central He-3 (détection active de neutrons) avec sept coques en polyéthylène haute densité qui peuvent être disposées autour du détecteur à la manière d'une poupée russe. Les spectres de neutrons issus des faisceaux de protons ont été mesurés à l'aide d'une version modifiée du NNS™ incorporant une coque de modérateur en laiton pour fournir une gamme d'énergie étendue (EER) pour la détection de neutrons à haute énergie. Les données de neutrons brutes ont été déployées en utilisant la méthode Maximum a Posteriori (MAP) (langage C++) et les fonctions de réponse du modérateur fournies par le fournisseur du NNS™. Notons que le MAP est une version modifiée de la

méthode d'estimation de la vraisemblance maximale (MLEM) qui pénalise tout composant à haut niveau de bruit. Pour tracer le flux des neutrons secondaires en fonction de l'énergie, la librairie d'analyse de données ROOT du CERN a été utilisée. En outre, les coefficients de conversion de l'ICRP ont été utilisés pour calculer les taux de la dose équivalente ambiante des neutrons générés autour des faisceaux d'électrons et de protons.

L'effet de plusieurs paramètres sur le flux des neutrons secondaires et sur le taux de la dose équivalente de ces neutrons a été étudié pour chaque situation de faisceau primaire.

Par rapport aux faisceaux d'électrons, on a observé que lorsque l'énergie du faisceau d'électrons primaires augmente, le flux des neutrons et le taux de la dose équivalente augmentent. En outre, la présence d'un fantôme d'eau solide dans le faisceau d'électrons primaires n'affecte pas les spectres de neutrons. Cependant, lors de la fermeture des mâchoires dans la tête de traitement, le flux des neutrons et le taux de la dose équivalente augmentent de manière significative ce qui signifie que la majeure production de neutrons secondaires autour des faisceaux d'électrons se passe dans l'accélérateur linéaire

Pour les faisceaux de protons, on a observé que lorsque l'énergie du faisceau de protons primaires augmente, le flux des neutrons et le taux de dose équivalente augmentent. La présence d'un fantôme d'eau dans le faisceau primaire augmente significativement les pics directs et d'évaporation des spectres de neutrons ce qui peut signifier qu'une partie importante de la production des neutrons secondaires autour des faisceaux de protons se passe dans le corps du patient. Le pic direct et celui d'évaporation du spectre de neutrons dominent le pic thermique lors de la mesure sur la table de traitement (près de la source de neutrons), tandis que le pic thermique domine lors de la mesure dans la jonction du labyrinthe (loin de la source de neutrons).

Mots clés : Neutrons secondaires, électrons, protons, MLEM, MAP, ROOT, flux de neutrons, taux de la dose équivalente.

Contribution of the author

The author certifies that he executed the total writing of all the thesis chapters.

Chapter 1:

The author did the literature research of all the discussed topics and performed the writing of this chapter sections.

Chapter 2:

The author wrote this chapter entirely based on his literature research.

Chapter 3:

The author wrote completely the code used in unfolding the experimental data and performed the experimental work around electron beams. In addition, the author contributed completely to the writing of this chapter.

Chapter 4:

The data was analyzed and the graphs were executed completely by the author. In addition, the author contributed entirely to the writing of this chapter.

Georges Al Makdessi, PhD

Table of contents

List of tables

CHAPTER 4

List of figures

CHAPTER 1

CHAPTER 2

CHAPTER 3

CHAPTER 4

Chapter 1: Introduction

1.1: What is cancer and how it is treated?

1.1.1: Cancer description

Cancer is an abnormal and out-of-control cell growth that can start anywhere in the human body and has the potential to invade or spread to other parts of the body. As malignant tumors grow, some cancer cells can break off and travel in the body through the blood or the lymph system and form new tumors far from the original one. The process by which cancer cells spread to other parts of the body is called metastasis.

Cancer is a genetic disease, mainly caused by mutations of three types of genes: proto-oncogenes, tumor suppressor genes, and DNA repair genes. The mutations that cause cancer can be inherited from our parents or can be caused by damage to DNA because of certain environmental exposures such as chemicals and radiation [1].

Proto-oncogenes are involved in normal cell growth and division. However, when these genes are altered or are more active than normal, they become oncogenes (cancer-causing genes) allowing unwanted cell growth and survival.

Tumor suppressor genes are also involved in controlling cell growth and division. Cells with certain alterations in tumor suppressor genes may divide in an uncontrolled manner.

Repair of damaged DNA is maintained by DNA repair genes. Cells with mutations in these genes tend to develop additional mutations in other genes.

1.1.2: Cancer treatment modalities

Chemotherapy

Chemotherapy (also called chemo) is a type of cancer treatment that uses drugs to kill cancer cells. Chemotherapy stops or slows down the growth of cancer cells, which grow and divide quickly. Chemotherapy may be used to make a tumor smaller before radiotherapy. This is called neoadjuvant chemotherapy. Adjuvant chemotherapy, on the other hand, consists of destroying cancer cells that may remain after treatment with surgery or radiotherapy. In addition, when chemotherapy is given at the same time of radiotherapy, we call it concomitant chemotherapy.

Chemotherapy not only kills fast-growing cancer cells, but also kills or slows the growth of healthy cells that grow and divide quickly. Damage to healthy cells may cause side effects, such as mouth sores, nausea, and alopecia.

Surgery

Surgery for tumor excision may be open or minimally invasive. In open surgery, the surgeon makes one large cut to remove the tumor, some healthy tissue, and sometimes some nearby lymph nodes. In minimally invasive surgery, the surgeon makes a few small cuts instead of one large one. The goal of surgery is to completely remove the cancerous tissue from the body. Complete excision, however, is not always possible and surgery may be followed by radiation to the tumor bed and chemotherapy to kill any remaining microscopic disease.

1.1.3: Radiotherapy

Radiotherapy is a cancer treatment that uses high doses of radiation to kill cancer cells and shrink or destroy tumors. The two main types of radiotherapy are external beam radiotherapy and brachytherapy.

Radiotherapy may be given before surgery, to shrink the size of the cancer, during surgery (intraoperative radiotherapy), or after surgery to kill any microscopic cancer cells that may remain. Radiation may also be given before, during, or after other cancer treatments to shrink the cancer or to kill any cancer cells that might remain.

During radiation delivery to cancer cells, nearby healthy cells are affected. Damage to healthy cells can cause side effects. These effects may show up directly (acute side effects) or may show up months or years after radiation delivery (late side effects). Medical staff (physicians, medical physicists, dosimetrists) try to protect healthy cells during treatment by aiming high doses of radiation at cancer while minimizing the amount of radiation that reaches nearby healthy tissue.

1.2: Radiation

1.2.1: What is ionizing radiation?

Ionizing radiation consists of particles, X-rays or γ-rays that have sufficient energy to eject electrons from the matter they encounter. Ionization of matter occurs through eight methods: the photoelectric effect, Compton scattering, and triplet production involving photons, the Auger effect, electron capture, and internal conversion, which are the result of internal rearrangements

within the atom or the nucleus, and Coulomb interaction and positron annihilation that result from the interaction of charged particles with the atom [2].

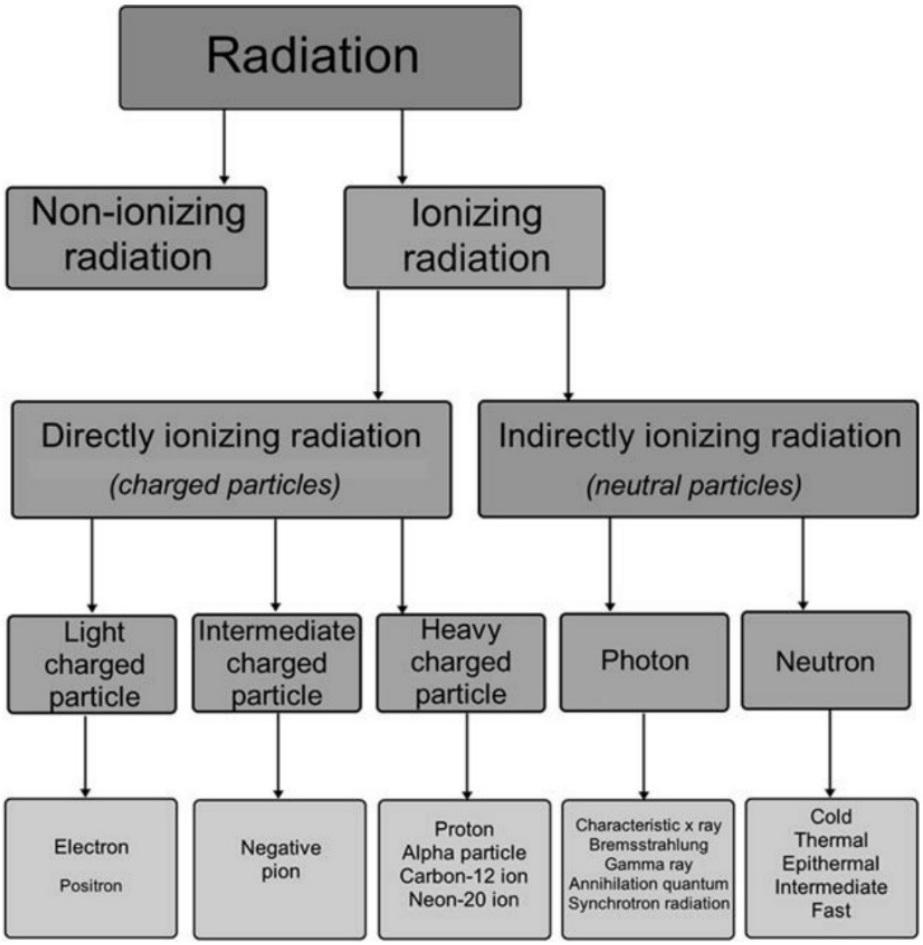

Figure 1.1 Classification of radiation [3].

Ionizing radiation ultimately deposits part or all of its energy into matter through Coulomb interactions. Energy transfer can be direct or indirect. Direct energy transfer results from the interaction of charged particles (electrons, positrons, muons, pions, protons and heavy ions) with matter. Indirect energy transfer is a two-step process, it happens when first a neutral particle (photon, neutron) interacts with matter to produce a charged particle that in turn undergoes Coulomb interactions. The classification of radiation is shown in Fig. 1.1.

Ionizing radiation is classified by its place of origin, i.e. nuclear or non-nuclear radiation. Nuclear radiation includes alpha, beta and γ-rays plus internal conversion electrons. Ionizing photons produced outside of the nucleus are referred to as X rays, to distinguish them from γ-rays, which arise within the nucleus. Beams of non-nuclear particulate radiation are typically labelled according to the particles that comprise them, for example proton beams or carbon-ion beams [2].

1.2.2: Radiation carcinogenesis

Ionizing radiation may cause initial injury at the microscopic level when absorbed in biological systems. In some cases, the microscopic damage may be repaired and go unnoticed, in other cases, it may ultimately manifest itself macroscopically as an observable effect. Macroscopic effects may result from a large radiation exposure that causes sufficient microscopic damage to be noticeable at the macroscopic level (deterministic effects), or they may be the propagated long-term consequences of just a single radiation-induced error in the genetic code (stochastic effects). The latter entailing radiation-induced carcinogenesis [2]. Note that the lowest acute dose causing cancer is known to be 100 mSv, while 1000 mSv, if received within 24 hours, is the dose causing radiation sickness. Receiving more than 5000 mSv at once may lead to death.

Radiation incident on a cell may directly or indirectly damage the DNA of the cell (Fig. 1.2). Direct action occurs when an ionizing particle interacts with and is absorbed by the DNA, which is damaged, initiating the events that lead to biological changes. Indirect action involves the absorption of ionizing radiation in the medium in which the DNA is suspended. Through a complex set of reactions, free radicals can be formed that can cause damage to the DNA.

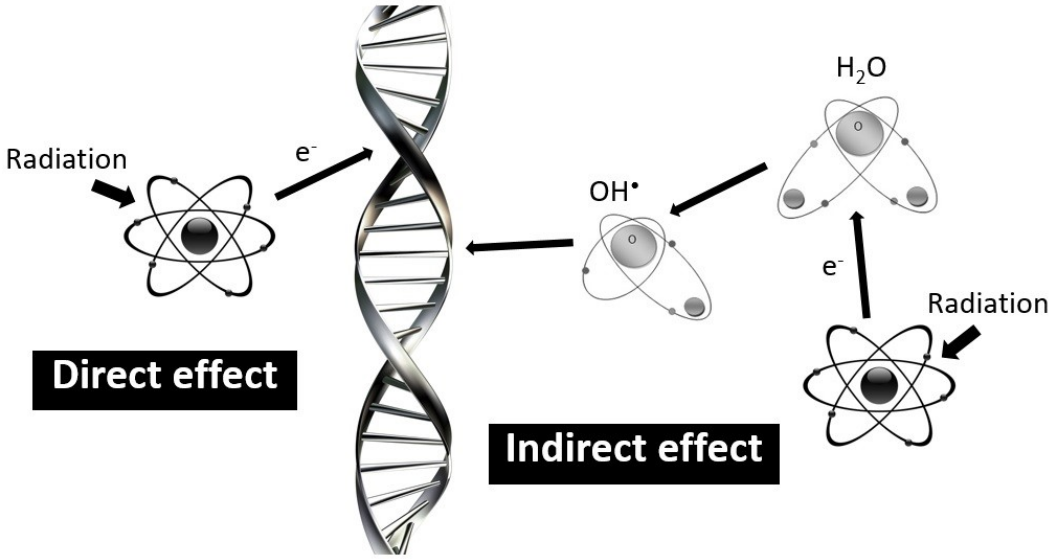

Figure 1.2 Representation of the direct and indirect effect of ionizing radiation on DNA.

1.2.3: Radiation protection

The three tenets underlying the physics of radiation protection are: distance, time, and shielding [2].

1. The distance from a radiation source should be maximized.
2. The duration of an exposure should be minimized.
3. The amount of shielding around a radiation source should be maximized and optimized. Radiation beams loose energy (by ionizations and excitations) and so are attenuated on passing through material. The level of attenuation depends on the type and energy of the radiation beam and the atomic number and density of the absorbing material.

Note that the effective dose limit for nuclear energy workers is 50 mSv for one full year and 100 mSv for five years, while it is equal to 4 mSv for pregnant nuclear energy workers during their

pregnancy period. In parallel, the effective dose limit is equal to 1 mSv for general population for one calendar year.

The ALARA principle

The ALARA principle is central to radiation protection. It stipulates that all/any exposure to ionizing radiation should be kept As Low As Reasonably Achievable, economic and social factors being taken into account.

1.3: External beam radiotherapy

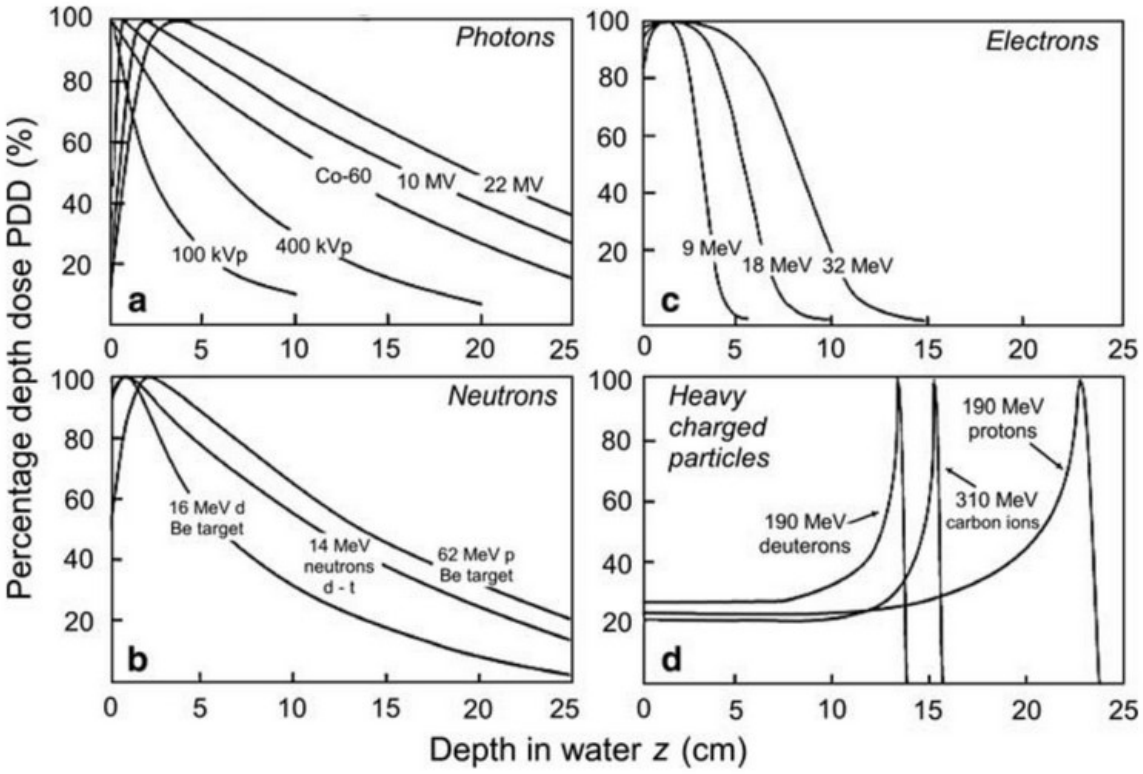

Figure 1.3 Percentage depth dose against depth in water for radiation beams of various types and energies [3].

In external beam radiotherapy, the radiation source is at a certain distance from the patient and the target within the patient is irradiated with a radiation beam arising from the source. As radiation enters the patient, the absorbed dose reaches a maximum at a certain depth. Note that the absorbed dose is defined as the mean energy imparted by ionizing radiation to a mass of matter in a finite volume. Its unit is J/kg or gray (Gy). The change in absorbed dose as a function of depth can be described by a quantity known as the percent depth dose (PDD) curve. The percent depth dose at a particular depth is defined as the absorbed dose at that depth normalized to the maximum dose. The PDDs corresponding to several types of radiation are shown in Fig. 1.3.

1.3.1: Photons

All photon beams are characterized by the same physical parameters but fall into various categories depending on their origin, means of production, and energy. With regard to the origin of photon beams we are dealing either with γ-rays that originate from radioactive nuclei or with x rays that originate in a target bombarded with energetic electrons. The X-rays from a target consist of bremsstrahlung photons and characteristic photons [3].

Photons can be used in several different types of external beam radiotherapy. These include orthovoltage radiation therapy, 3D conformal radiation therapy, Intensity Modulated Radiation Therapy (IMRT), volumetric modulated arc therapy (VMAT), and stereotactic radiation therapy, also known as radiosurgery (GammaKnife, CyberKnife) or SBRT. Most of these techniques involve the use of machines called linear accelerators, or "linacs" [4].

1.3.2: Electrons

Linear accelerators, in addition to producing ionizing photon beams, can also produce electron beams. Electrons lose most of their energy near the surface of the absorber (i.e. the skin) and are commonly used to treat superficial tumors [4].

1.3.3: Protons

Proton therapy utilizes protons to deliver ionizing radiation to a target while minimizing dose to nearby organs. The advantage of protons compared to other forms of radiation is that the depth at which they deposit their energy can be precisely controlled (Fig. 1.4).

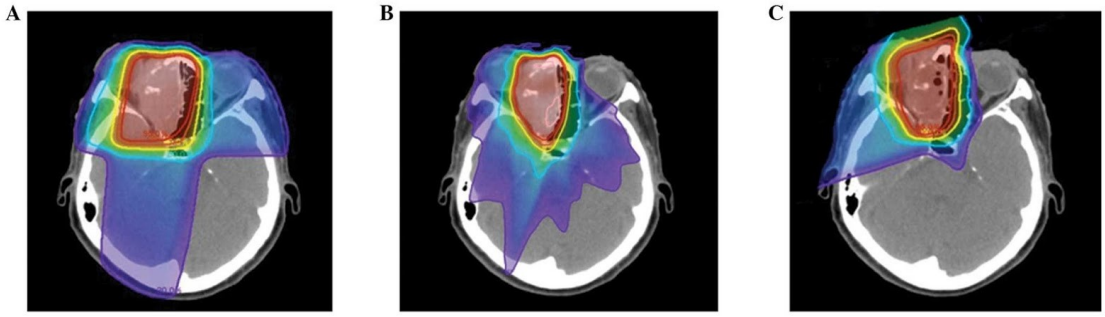

Figure 1.4 Comparison of dose distributions according to the treatment method: a) three-dimensional conformal radiation therapy, b) intensity-modulated radiation therapy, c) proton beam therapy [5].

As a proton enters the body, it releases small amounts of energy, and slows down. At the end of its path, it releases a large amount of energy (known as the Bragg peak), and very little energy is released past that point. Using computer software and appropriate energy modulation, proton

beams can be directed to release most of their energy precisely within the tumor, with very little of the energy exiting out of the back of the tumor. Hence, if the back edge of the tumor is located against the spinal cord, for example, it may be possible to spare any radiation dose to the spinal cord using protons [4].

1.3.4: Neutrons

In comparison with photon and electron beams, the main attraction of fast neutron beams in external beam radiotherapy is their much lower oxygen enhancement ratio (OER). The OER is defined as the ratio of doses without and with oxygen (hypoxic vs. well-oxygenated cells) to produce the same biological effect. The OER for electrons and photons is about 2–3 while for neutrons it is only about 1.5. Note that the presence of oxygen in a cell acts as a radiosensitizer, making the effects of the radiation more damaging. Human solid tumors are invariably less well-oxygenated than the normal tissues, which is so-called tumor hypoxia leading to resistance to radiotherapy.

1.3.5: Heavy ions (carbon ions)

Carbon ion radiation can be helpful in treating cancers that do not usually respond well to radiation (called *radioresistant*). It is also called *heavy ion radiation* because it uses particles that are heavier than protons. Because they are so heavy, they can do more damage to the target cell than other types of radiation. As the mass of the radiating particles increases, the linear energy transfer (LET) to the medium that they are passing through increases as the cross section for

interaction rises resulting in a higher probability of causing clustered DNA damage. The main reason for using heavy charged particles in radiotherapy is their favorable depth-dose curve (Bragg peak) [6]. A comparison of depth-dose curves for electromagnetic radiation (Cobalt gamma and megavolt photon beams) and carbon ion beams is displayed in figure 1.5.

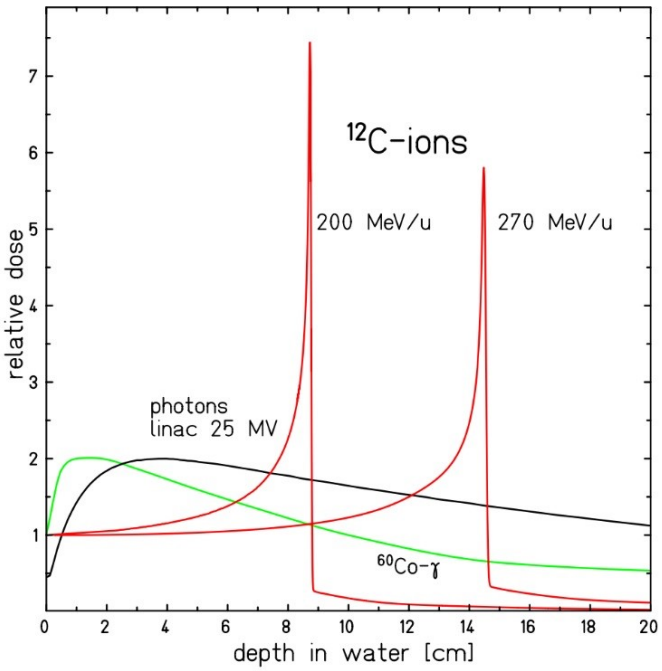

Figure 1.5 Depth-dose curves of ^{60}Co radiation, megavolt photons and ^{12}C ions in water [6].

1.4: Scope of the thesis

In radiation therapy with high-energy photon and electron beams (E > 10 MeV), secondary neutrons are generated via the photonuclear interaction. These neutrons affect the shielding requirements in radiation therapy rooms and also pose a health risk for patients undergoing high-energy radiation therapy because they increase the out-of-field radiation dose and, thus, the corresponding risk of iatrogenic radiation-induced malignancies.

In order to evaluate the biological effects of secondary neutrons (probability of cancer induction and genetic damage) on the human body, their fluence rate around clinical high-energy beams must be determined as a function of energy (neutron spectroscopy), since the ICRP radiation weighting factors (see Figure 1.6) for stochastic effects of neutrons are dependent on their energies. Note that the particle fluence is the number of particles crossing unit area. The particle fluence rate or the particle flux is defined as the particle fluence per unit time. For a monoenergetic beam, the energy fluence is the product of the beam energy and the particle fluence. The principle of the weighting factor will be discussed in the following chapters.

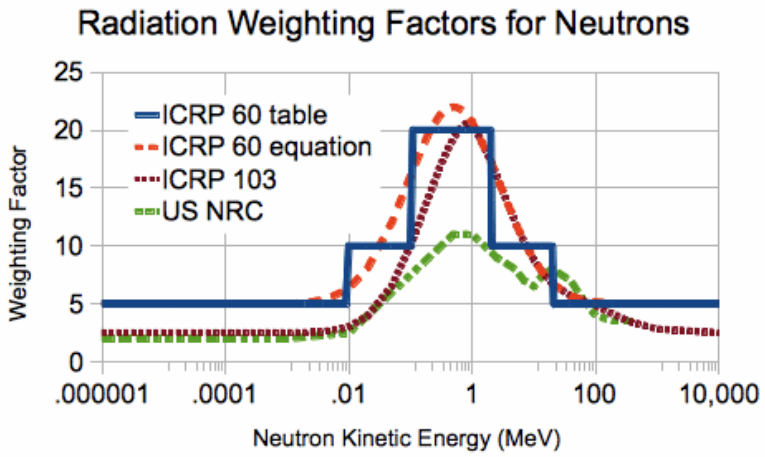

Figure 1.6 Neutron radiation weighting factor as a function of neutron kinetic energy [7].

In the research project reported in this thesis, a study was carried out to measure secondary neutron spectra around clinical electron and proton beams, using a Nested Neutron Spectrometer (NNS™) [8] and an appropriate spectral-unfolding method in order to determine the ambient dose equivalent due to these neutrons, which leads to the evaluation of the radiation risk related to these secondary particles on the patient and the staff. This research was motivated by the availability of an NNS™ at McGill University. The NNS™ offers a practical and convenient

method to study neutrons around radiotherapy beams. In particular, as there were no comprehensive reports in the literature detailing the energy spectra of electron beams, the NNS™ offered an opportunity to quantify these spectra. Furthermore, as the NNS™ had not been previously used to measure neutron spectra around proton beams, it was considered appropriate to examine its usefulness in this context of protons. Finally, although the NNS™ allows for the measurement of neutron spectra, any clinically-relevant information regarding carcinogenic risk is dependent on the ICRP weighting factors, as discussed in this thesis. Thus, the second goal of this thesis was to understand the energy dependence of the neutron weighting factor by using Monte-Carlo simulations.

Chapter two presents the physical aspects of neutrons such as their classification in terms of energy, their interactions with matter, the methods used to detect them and their generation in high-energy clinical beams. Chapter three describes the experimental setup and the unfolding methods used to generate the neutron spectra reported here using the NNS™. Chapter four presents the experimental results including the verification of the spectral changes with respect to the beam size, the beam energy, the position relative to the beam, and the presence of a plastic phantom, in addition to a Monte Carlo analysis concerning the neutron weighting factors. Finally, chapter five offers a conclusion and a discussion of the findings of this research.

Chapter 2: Neutrons and their Detection

This chapter is intended to provide a theoretical review of neutrons. In detail, we present a full description about their energies, their interactions (cross sections) and their detection.

2.1: What are neutrons?

Neutrons are elementary neutral particles. Neutrons can be bound inside the nucleus or can be free. Free neutrons are unstable and have a half-life of about 10 minutes. An unstable free neutron undergoes beta decay by transforming into a proton, an electron and a neutrino. Free neutrons are classified according to their kinetic energy [9]: Cold Neutrons (0 eV to 0.025 eV), Thermal Neutrons (about 0.025 eV), Epithermal Neutrons (0.025 eV to 0.4 eV), Cadmium Neutrons (0.4 eV to 0.5 eV), Epi-cadmium Neutrons (0.5 eV to 1 eV), Slow Neutrons (1 eV to 10 eV), Resonance Neutrons (10 eV to 300 eV), Intermediate Neutrons (300 eV to 1 MeV), Fast Neutrons (1 MeV to 20 MeV) and Relativistic Neutrons (Higher than 20 MeV). Note that thermal neutrons are in thermal equilibrium with their surrounding medium. Due to their relatively high effective absorption cross-section, thermal neutrons play an important role in neutron activation of atoms.

2.2: Neutron interactions with matter

Nuclei are the principal target in an absorber atom with which free neutrons interact since they are neutral particles and no Coulomb interaction is involved. In addition, neutrons deposit their

dose indirectly in a medium, similarly to photons, via an intermediate step involving the creation of charged particles which in their turn deposit the radiation dose [3].

Neutrons interact with the nuclei of the absorber by five principal processes: (1) Elastic scattering, (2) Inelastic scattering, (3) Neutron capture, (4) Nuclear spallation and (5) Nuclear fission. Cross sections (expressed in barns or 10^{-28} m^2) are used to describe the probability of interaction between an incident neutron and a target nucleus [9]. The neutron cross section depends on the target nucleus, the type of the reaction, the neutron energy and the target energy.

Neutron capture is one of the most common neutron interactions. Neutron capture occurs when a thermal neutron is captured by a nucleus leading to the emission of a proton or a γ ray. Two neutron capture interactions are of particular importance in tissue: 14 N (n, p) 14 C and 1 H (n, γ) 2 H and two interactions: 113 Cd (n, γ) 114 Cd and 10 B (n, α) 7 Li are of importance in shielding against thermal neutrons. Some absorber nuclei may undergo a fission event after neutron capture, leading to two or more fission fragments and a few neutrons. Usually, the door shielding in a therapy room consists of a layer of borated paraffin and a layer of polyethylene. Borated paraffin slows down the neutrons and polyethylene undergo neutron capture. In the case of doorless therapy rooms, polyethylene layers are fixed on the walls of the maze connecting the therapy room to the console room. These layers provide the moderation and the capture of the secondary neutrons.

2.3: Neutron detection

2.3.1: Slow neutron (< 0.5 eV) detection methods

2.3.1.1: BF_3 proportional tube

The BF_3 proportional tube is extensively used as a detector of slow neutrons (An example is shown in Fig. 2.1) where BF_3 serves as target for slow neutron conversion into secondary particles and as proportional gas. To increase the efficiency of these detectors, BF_3 is highly enriched in 10B. The absolute pressure in typical tubes is limited to about 0.5-1.0 atm because the performance of BF_3 is poor when operating at higher pressures [10].

Figure 2.1 Boron trifluoride (BF_3) proportional counters [11].

2.3.1.2: Boron-lined proportional counters

In order to use a more suitable proportional gas than BF_3, the interior walls of the proportional tube can be coated by solid boron. Actually, the increase in the boron-coated surface area results in higher neutron sensitivity. In addition, by using alternative gases, the chemical degradation problems in BF_3 can be greatly reduced when exposed to high γ-ray fluxes [10].

2.3.1.3: Boron-loaded scintillators

In order to circumvent the limitation of the BF_3 proportional tubes due to the uncertainty in defining the point of interaction of the neutron in the volume occupied by the BF_3 fill gas, scintillators were made by fusing B_2O_3 and ZnS [10].

2.3.1.4: He-3 proportional counters

The He-3 proportional counters are widely used for slow neutron detection because of the high cross section of the 3He (n, p) H reaction. To fabricate an efficient detector, high purity 3He must be used because helium is a noble gas and it can't be used in the solid state. Note that the range of the secondary particles (protons and tritons) created by the interaction of thermal neutrons with 3He atoms is usually larger than the dimensions of the proportional tube. This leads to an important wall effect in these proportional counters. To minimize the wall effect, the range of tritons and protons must be lowered by enhancing their stopping power. This is generally done by increasing the pressure of the 3He gas or by adding a small amount of a heavier gas to the 3He to provide an enhanced stopping power like Krypton for example [10].

2.3.2: Fast neutron detection

When the neutron energy increases, the neutron interaction cross sections in any slow neutron detector decrease rapidly. The detection efficiency of high energy neutrons can be improved by surrounding the detector with hydrogen-containing moderating materials (see Fig. 2.2). When passing through the moderator, the high energy neutron loses its kinetic energy by elastic

scattering interactions and reaches the detector with a lower energy which will increase its detection efficiency by the detector. By increasing the thickness of the moderator, the fast neutron undergoes more collisions and loses more of its kinetic energy which enhances the detection efficiency. On the other hand, making the moderator thicker will lead to a lower probability that an incident fast neutron reaches the detector. Note that for polyethylene or paraffin, for example, the optimum thickness of the moderator ranges from a few centimeters to several tens of centimeters depending on the incident neutron energy [10]. In addition, by changing the thickness of the moderator around the detector and perform a measurement after each change, we can easily quantify the energy spectrum of a poly-energetic neutron beam.

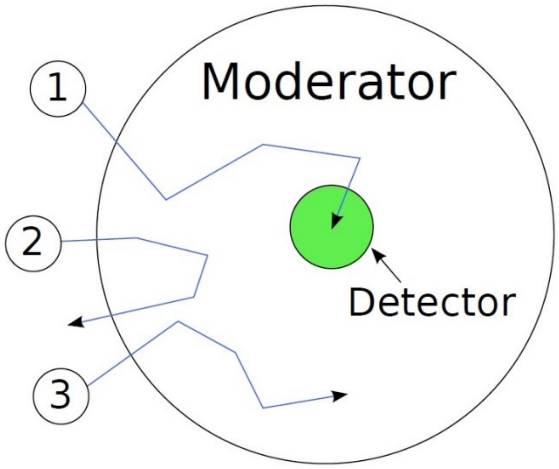

Figure 2.2 Neutrons inside a moderator. Neutrons (1) are moderated and detected. Neutrons (2) are moderated but escape. Neutrons (3) are absorbed by the moderator [12].

2.3.2.1: Bonner sphere spectrometer

A Bonner sphere spectrometer (BSS) is used to determine the energy spectrum of a neutron beam. This device was invented by Bramblett, Ewing and Tom W. Bonner [13] and is based on a

thermal detector embedded in a set of polyethylene moderating spheres of different sizes, and the associated electronics in the case of an active detector like 3BF, 3He or scintillators (Fig. 2.3). The BSS is applied to characterise the neutron field from thermal energies to hundreds of MeV where the comparison of the neutrons detected by each sphere allows accurate determination of the neutron energy. One of the main advantages of the BSS system is its isotropic response to neutrons resulting from its spherical symmetric shape [14].

Figure 2.3 Presentation of a Bonner sphere spectrometer.

2.3.2.2: Bubble detectors

Bubble detectors provide an immediate measurement of neutron hazards making them ideal for radiation protection. Note that a radiation dosimeter measures ionizing radiation quantities such as exposure, kerma, absorbed dose and equivalent dose while a radiation detector is used to detect, track and identify ionizing particles. A bubble detector comprises a superheated liquid consisting of tiny droplets embedded in a polymer tube. When an incident neutron collides with one of the liquid droplets, the droplet transforms into a visible gas bubble. The tissue-equivalent

neutron dose can be determined directly from the number of the formed droplets in the detector (see Fig. 2.4).

Figure 2.4 Neutron bubble detectors [15].

2.4: Secondary neutron generation around external-beam radiotherapy beams

The main generation of secondary neutrons around external-beam radiotherapy beams lies in the treatment head of the linear accelerators (linacs) including the walls of the vacuum chamber, the walls of the waveguide, the x-ray target, the beam extractor, filters, collimators, transmission ionisation chambers and light localizers (a schematic of a medical linear accelerator is shown in Fig. 2.5). Note that the main components in the treatment head are 184W, 208Pb and 27Al. Other sources of secondary neutrons include the patient (1H, 16O, 12C and 14N), the air (16O and 14N) and the borated concrete walls of the bunker (1H, 16O, 28Si, 40Ca, 12C, 10B and 11B).

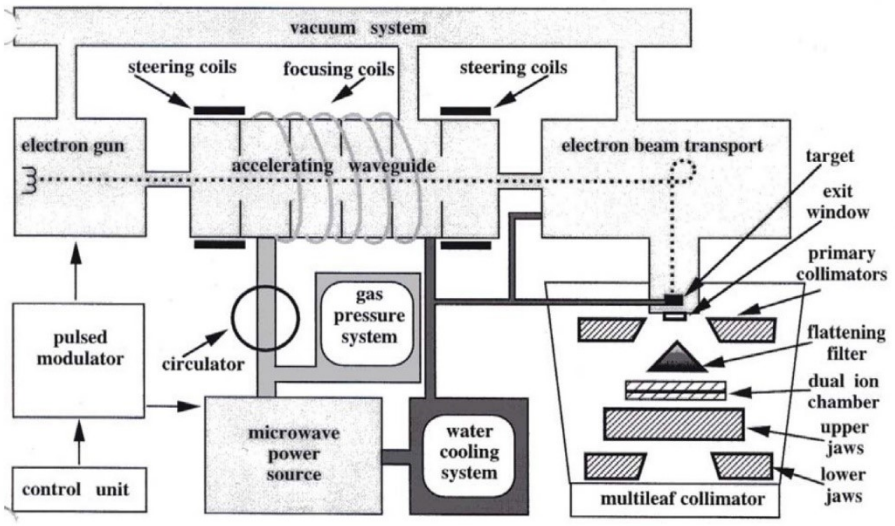

Figure 2.5 Schematic diagram of a medical linear accelerator [16].

2.4.1: Photon beams

Two quantities govern the photoneutron production: the neutron separation energy and the photoneutron cross section.

The neutron separation energy is the threshold energy for the interaction between the photon and the neutron to occur. For example, the photoneutron production for W and Pb has a threshold energy of 6.74 and 6.19 MeV, respectively, while its threshold energy is equal to 1.22 MeV for beryllium. Alternatively, the photoneutron cross section increases steeply with photon energy and reaches its maximum value for a photon energy of 13–18 MeV for the materials used in the linac head including W, Pb, Cu and Fe.

Secondary neutron spectra from photon therapy have three pronounced peaks. The first peak is comprised of direct neutrons and ranges from approximately 10 MeV to the maximum photon energy. The second peak is due to evaporation processes and is located at an energy around 1 MeV. The third is a thermal peak due to neutrons that have scattered around the room before

arriving at the measurement location. Neutrons also exist between these peaks in the form of an intermediate energy continuum [17].

2.4.2: Electron beams

Secondary neutrons from electron beams or electro-neutrons are produced through a two-step process. First, the electron undergoes an inelastic scattering by the Coulomb field of a nucleus creating a virtual photon with energy h = Ei – Ef, where Ei and Ef are the electron energies before and after being scattered, respectively. Second, the virtual photon interacts with the nucleus to initiate the photodisintegration reaction [18]. Note that the main feature of the virtual photon is that is not independent of its source and does not satisfy E = pc, where E is the photon energy and p is the photon momentum [18].

Secondary neutron spectra from electron therapy have three pronounced peaks. The first peak is comprised of direct neutrons and ranges from approximately 10 MeV to the maximum electron energy. The second peak is due to evaporation processes and is located at an energy around 1 MeV. The third is a thermal peak due to neutrons that have scattered around the room before arriving at the measurement location. Neutrons also exist between these peaks in the form of an intermediate energy continuum [17].

2.4.3: Proton beams

As for high-energy photon and electron therapy (>10 MeV), the generation of secondary neutrons is an unavoidable consequence of proton therapy. These secondary neutrons have a

wide energy range, from thermal energies up to the maximum beam energy which is as high as 250 MeV at some centers. Secondary neutron spectra from proton therapy have the same three pronounced peaks as in case of photons and electrons: direct, evaporation and thermal.

2.4.4: Neutron dosimetry

Secondary neutrons pose a health risk for any patient undergoing high-energy radiation therapy because they increase the out-of-field radiation dose and, thus, the corresponding risk of secondary malignancies.

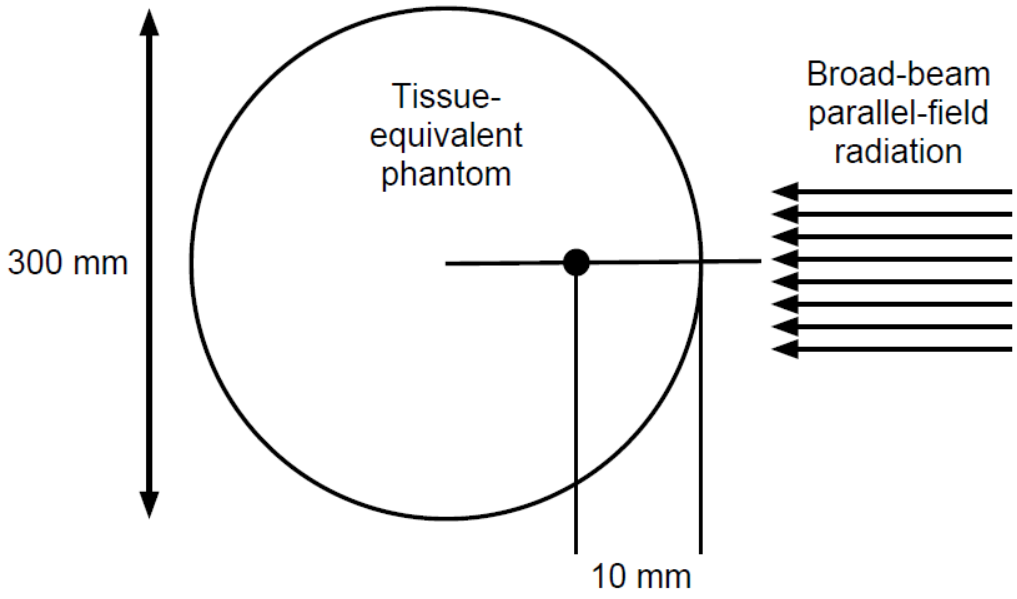

Figure 2.6 The ICRU sphere showing the dose delivery depths used in the definition of the ambient dose equivalent.

In order to evaluate the biological effects of the secondary neutrons (probability of cancer induction and genetic damage) on the human body, the ambient dose equivalent rate must be determined. The ambient dose equivalent, expressed in Sievert (Sv), is the dose delivered to a well-defined depth in the ICRU sphere from a broad-beam parallel-field irradiation. For strongly penetrating radiation a depth of 10 mm is used and for weakly penetrating radiation a depth of 0.07 mm is used, as shown in Fig. 2.6.

Since the weighting factor of neutrons is dependent on their energies, the fluence rate of the secondary neutrons must be determined as a function of energy (neutron spectroscopy). Then, the neutron ambient dose equivalent rate can be calculated through the following relationship:

$$H = \sum_E \varphi(E).h_\varphi(E) \tag{2.1}$$

Where H in units of mSv/h, $\varphi(E)$ is the energy dependent neutron fluence rate and $h_\varphi(E)$ is the fluence-to-dose equivalent conversion factor provided by the ICRP 74 report [19]. Note that a radiation weighting factor is an estimate of the effectiveness per unit dose of a given ionizing radiation. Weighting factors are dimensionless multiplicative factors used to convert physical dose (Gy) to equivalent dose (Sv) to place biological effects from exposure to different types of radiation on a common scale.

Chapter 3: Experimental Materials and Methods

3.1: Goals of experimental work

This experimental work aimed to better understand the production of secondary neutrons in radiation therapy so that ultimately their biological effects might be mitigated. This was done by applying a new spectroscopic method (using the Nested Neutron Spectrometer (see Fig. 3.1)) and unfolding algorithms, allowing the generation of energy dependent neutron fluence rates and the determination of neutron ambient dose equivalents for any exposure situation.

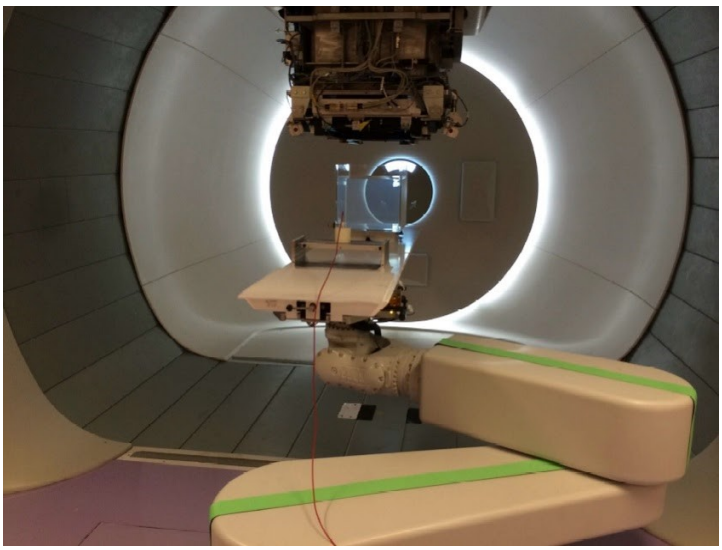

Figure 3.1 The NNS™ on the couch of the Skandion proton therapy beam with the water phantom in place.

More specifically, the scope of this thesis was to: (1) compare and verify the validity of two unfolding methods (MLEM and MAP), (2) study and evaluate the production of secondary neutrons around electron and proton clinical beams and (3) understand the physical aspects of ICRP neutron weighting factor.

3.2: NNS™ spectrometer

The Nested Neutron Spectrometer (NNS™) is a neutron spectrometer which consists of a He-3 detector sensitive to thermal neutrons embedded in seven cylindrical high-density polyethylene (HDPE) moderators that can be added or removed in Russian doll fashion (see Fig. 3.2 and Fig. 3.3). Each moderator is designed to mimic the response function of an equivalent Bonner sphere moderator [13]. After measurements have been made, an unfolding algorithm is executed in order to obtain 52-bin and 58-bin spectra of neutron energies corresponding to secondary neutrons from electron and proton beams respectively.

Note that when operating with proton beams, neutron spectra were measured using a modified version of the Nested Neutron Spectrometer, incorporating a brass moderator shell to provide an extended energy range (EER) for the detection of high-energy neutrons from the proton beams.

Figure from Dubeau et al., 2013, poster presentation CRPA conference, Sherbrooke, Quebec

Figure 3.2 The NNS™ detector and the moderators used in our measurements. The brass moderator is not shown.

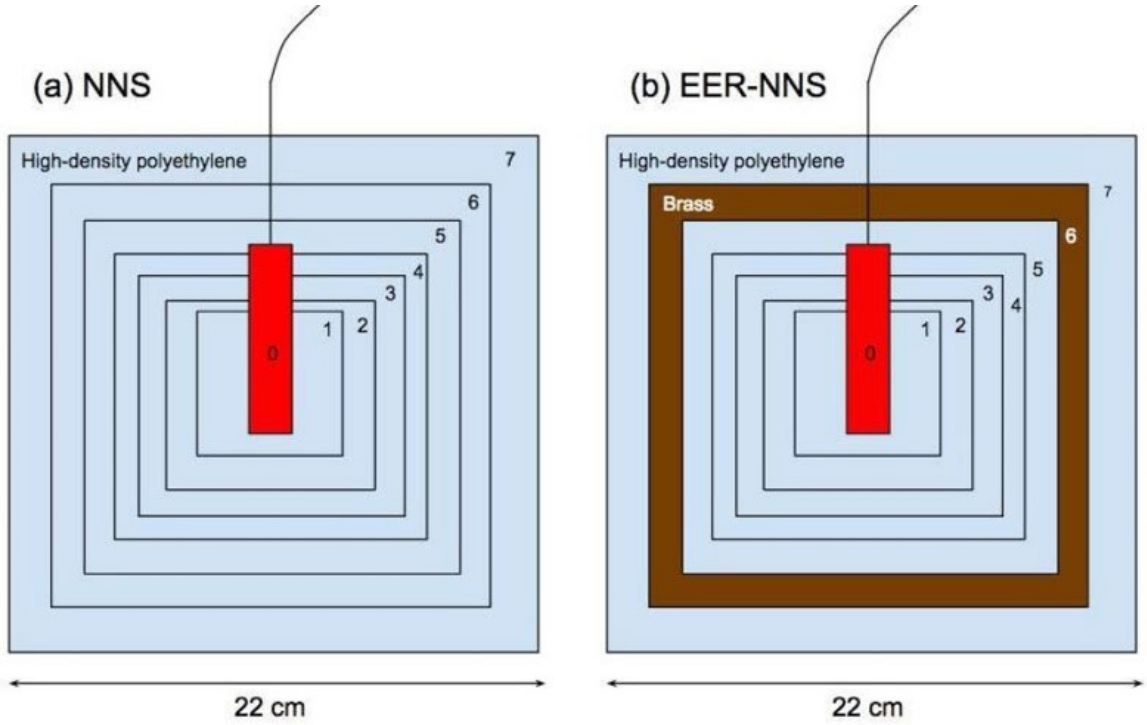

Figure 3.3 The standard NNS™ (a) and the extended energy range (EER) NNS™ [12]. Note that the helium detectors are embedded in the red cylinder marked 0 during measurements.

3.2.1: He-3 and He-4 detectors

Two types of gas-filled detector were used in our measurements: He-3 and He-4. These two detectors, used separately, are contained in a metallic shell and have an active diameter and length of 15.5 mm and 23.8 mm, respectively. The two detectors are biased at a voltage of 150 V in current-mode. The He-3 detector is pressurized to 2 atm with the addition of 0.7 atm of krypton as a quench gas. As described earlier, this increases the stopping power of the gas which decreases drastically the wall effect in the detector.

Note that the He-3 detector is used to perform all the neutron measurements but since this detector, when operated in current mode as described below, cannot discriminate photons, a He-4

detector is used to quantify the photon background. The He-4 detector is uniquely sensitive to photons and was tuned by the vendor to have the same photon response as the He-3 detector. By subtracting the reading of the He-4 detector from the main reading measured by the He-3, the photon background can be removed from the signal.

3.2.2: Moderators

The moderators are cylindrically-shaped HDPE shells that are added around the gas-filled detector. Each additional shell is added around the previous smaller combination of shells and sealed with a cap. To transmit the signal from the detector to the electronics, a small hole for a triaxial cable is drilled in the center of each cap.

Response functions for each moderator were determined by the vendor from Monte Carlo simulations of isotropic radiation incident on the NNS™. These were provided by the vendor with units of cm^2 and are used to obtain a fluence rate spectrum after unfolding.

3.2.3: Operation

The NNS™ was operated in current-mode, as an ionization chamber with an electrometer. In this mode, the measured current is converted to corresponding count-rate through a calibration coefficient supplied by the vendor, and previously confirmed by our research group [20], and having a value of 7 fA/(counts/s).

Before every measurement, a leakage test is performed to evaluate the magnitude of the leakage current which is then subtracted from the total charge after measurement. Then, the count-rate

combined with the response functions for each moderator allows us to calculate the neutron spectrum through mathematical unfolding (Fig. 3.4).

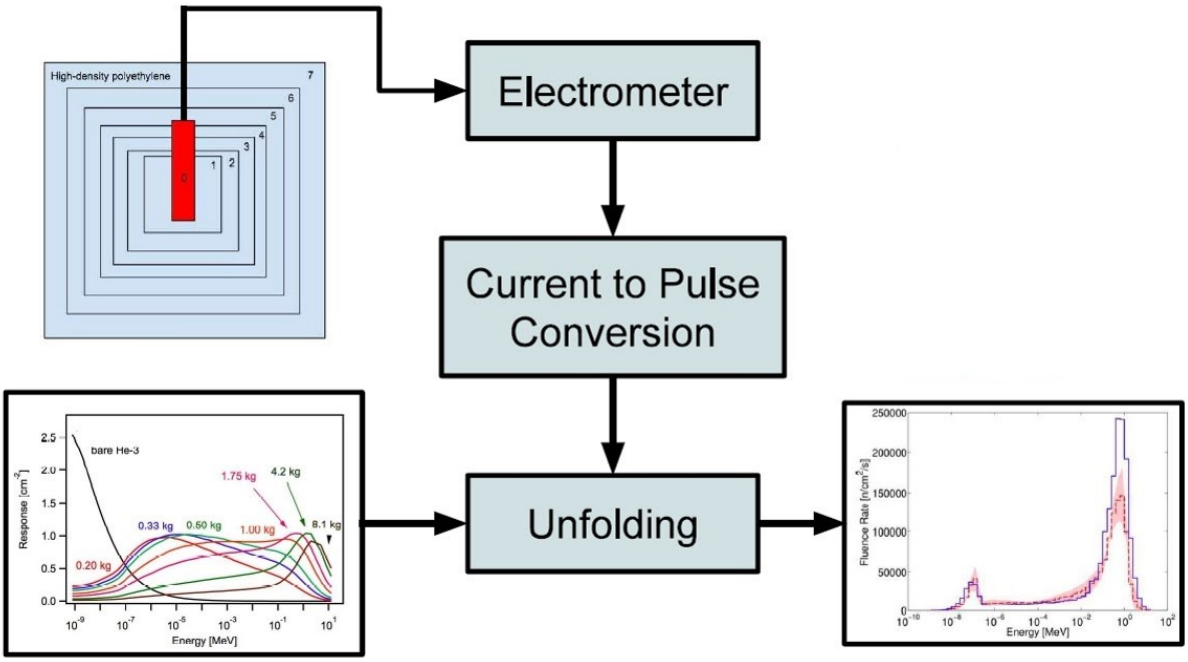

Figure 3.4 The performed procedure to get the secondary neutron spectra.

3.3: Unfolding methods

To unfold the raw data, we developed an algorithm by which we deconvolved the eight measurements, one per moderator and the bare detector, into a 52-bin neutron energy spectrum in case of electrons and the nine measurements into a 58-bin neutron energy spectrum in case of protons using the response function of each moderator provided by the vendor of the NNS™.

Note that the unfolding algorithm was written using the C++ language and the secondary neutron spectra were plotted using the ROOT library from CERN. Statistical uncertainties on the measurements were estimated using a random sampling process.

3.3.1: MLEM algorithm

Maximum-likelihood expectation-maximization (MLEM) is a standard statistical reconstruction tool that is commonly used in positron emission tomography (PET) image reconstruction. When applied to convergence, the MLEM algorithm maximizes the likelihood of obtaining the measured data *m* given that the spectrum is *n* and is described as follows [21]:

$$n_j^{k+1} = \frac{n_j^k}{\sum_{i=1}^{N} a_{ij}} \sum_{i=1}^{N} a_{ij} \frac{m_i}{\sum_{b=1}^{j} a_{ib} n_b^k} \tag{3.1}$$

Where n_b^k is the starting spectrum, n_j^k is the current spectrum estimate, a_{ij} is the response function of the detector and m_i is the measurement in counts per second.

MLEM is a straightforward algorithm and can be described as follows:

1) Create a guess spectrum n_b^1.
2) Convolve this spectrum with the detector response function.
3) Divide the measurement by the result and deconvolve.
4) Update the current estimate of the neutron spectrum.

Note that *i* in (3.1) belongs to one of the eight measurements, one per moderator and the bare detector, in case of electrons and to one of the nine measurements in case of protons, while *j* belongs to one of the 52 bins constituting the neutron energy spectrum in case of electrons and to one of the 58 bins constituting the neutron energy spectrum in case of protons. Note that the final number of iterations is defined as the number of times the previous procedure is performed. A disadvantage of the MLEM method is its tendency to produce noisy reconstructed data as the number of iterations increases.

3.3.2: MAP method

A variant of the MLEM algorithm is the maximum a posteriori (MAP) method, which differs from MLEM primarily by the introduction of a function E that penalizes any high noise component [21]:

$$n_j^{k+1} = \frac{n_j^k}{\sum_{i=1}^{N} a_{ij} + \beta \frac{\partial}{\partial n_i} E(n_i)} \sum_{i=1}^{N} a_{ij} \frac{m_i}{\sum_{b=1}^{j} a_{ib} n_b^k} \tag{3.2}$$

The adjustable parameter β determines the strength of the regularization term, and it can be seen that for $\beta = 0$ Eq. 3.2 becomes Eq. 3.1. Note that if the value of β is very small, MAP method converges to MLEM method and if its value is important, MAP gives nonsense results. Thus, the value of β was chosen in between these two extremes separately for each measurement. In addition, the term in the denominator of Eq. 3.2 which is multiplied by β represents the squared deviation of a data point n_i from the average of its neighborhood or the squared deviation from the neighborhood's median value:

$$\frac{\partial}{\partial n_i} E(n_i) = \sum_l (n_i - n_l)^2 \tag{3.3}$$

Where l indicates the two neighbor data points of the data point i. The first and last points have only one neighbor.

3.3.3: Dose equivalent rate calculation

Neutron ambient dose equivalent was determined from the unfolded NNS™ measurements. ICRP-74 fluence-to-dose coefficients [22] were used to convert the NNS™ energy-dependent neutron fluence rates into ambient dose equivalent.

Note that the uncertainty on the energy-dependent neutron fluence rates is calculated by first generating 1000 sets of eight test values from the eight measured values (raw data) using the Poisson distribution. Then, each set of the eight Poisson-generated test values was unfolded in the same way as the eight "real" measured values leading to 1000 sets of 52 "Poisson" values of fluence rate. The standard deviation values for each bin in the final spectrum were calculated by using the main unfolded data and the 1000 Poisson-unfolded test data. Finally, propagation of errors was used to calculate the uncertainty on the value of the ambient dose equivalent.

3.4: Validity of the use of the NNS™

Our group has evaluated the performance of the NNS™ in terms of reproducibility, linearity, and dose-rate effects in a bunker housing a Varian Clinac 21EX at the Montreal General Hospital in previously-published work (Maglieri et al 2015 [20]). Using the MLEM algorithm, measured secondary neutron spectra around clinical photon beams at various locations inside the bunker were compared to Monte Carlo simulations of an identical setup. In terms of dose, neutron ambient dose equivalents were calculated from the measured spectra and compared to bubble detector neutron dose equivalent measurements.

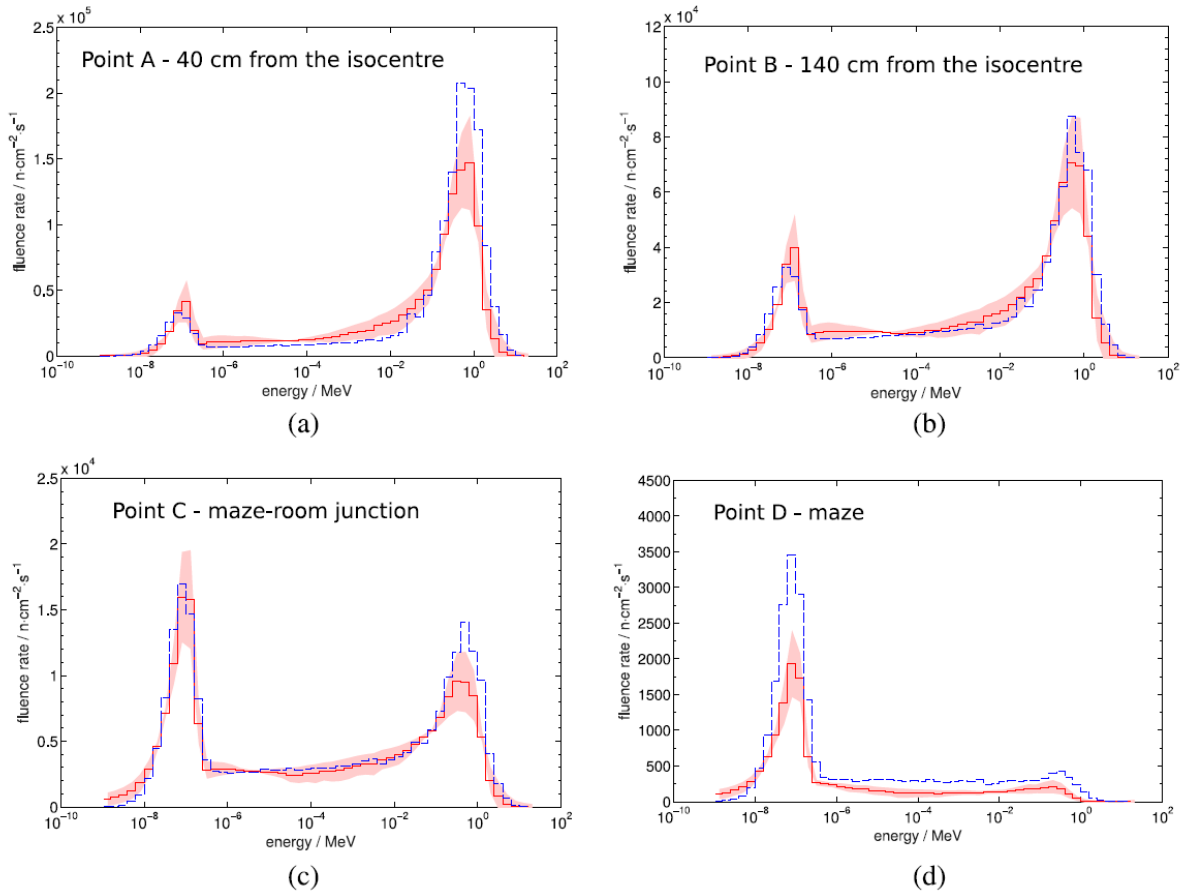

Figure 3.5 Measured (solid) and simulated (dashed) neutron spectra at different points in the bunker of a Varian 21EX at the Montreal General Hospital. The shaded region is the statistical uncertainty associated with the measurement [20].

Our group found that the neutron fluence-rate decreased with distance from the source and the shape of the spectrum changed from a dominant fast neutron peak near the Linac head to a dominant thermal neutron peak in the moderating conditions of the maze. Monte Carlo data and NNS™-measured spectra agreed within 30% at all locations except in the maze where the deviation had a maximum of 40%. In addition, neutron ambient dose equivalents calculated from the measured spectra were consistent with bubble detector measurements in the treatment room. This clearly indicates that the NNS™ may be used to reliably measure secondary neutron spectra around radiotherapy beams.

3.5: Description of the facilities

3.5.1: Electron facility

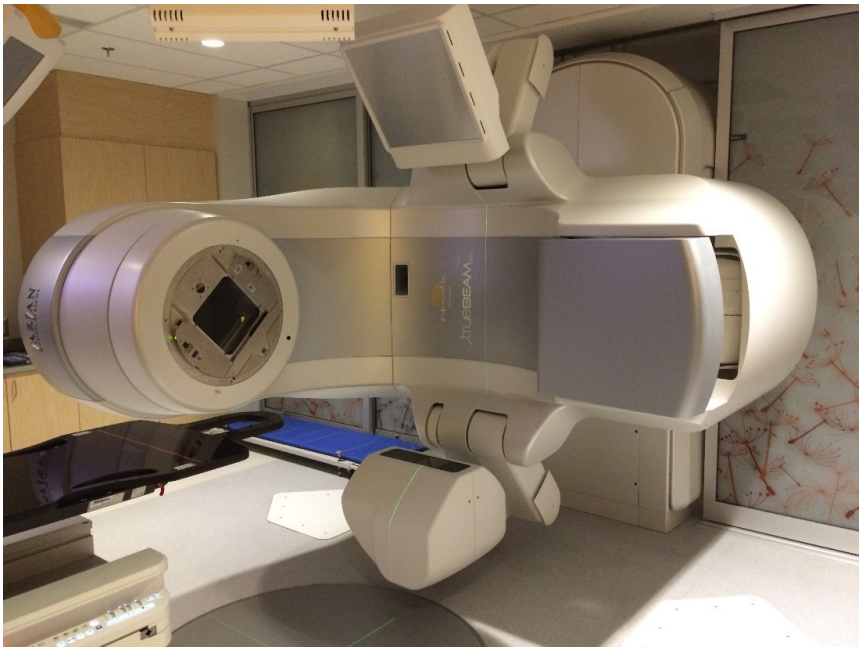

Figure 3.6 The Varian medical linear accelerator at the Cedars Cancer Centre in Montreal, Canada.

Neutron spectra were measured for secondary neutrons arising from a clinical electron beam in a treatment room equipped with a Varian linear accelerator with maximum electron energy of 20 MeV at the Cedars Cancer Centre in Montreal, Canada (see Fig. 3.6).

3.5.2: Proton facility

Neutron spectra were measured for secondary neutrons arising from a clinical proton beam in a treatment room with a gantry and a dedicated nozzle at the Skandion proton therapy clinic in Uppsala, Sweden (see Fig. 3.7). The beam was generated by the compact IBA Proteus Plus cyclotron with maximum proton energy of 230 MeV.

Figure 3.7 The proton facility at the Skandion proton therapy clinic in Uppsala, Sweden.

3.6: Description of the setups

All the performed measurements were done out of the primary radiation beam field. The primary beam is defined by the field size of the beam itself, while the out-of-field beam consists of the leakage from the treatment head of the linear accelerator and from the scatter from the collimator and from the patient body.

In the case of electron beams, the Linac was operated at 3 energies: 12, 16 and 20 MeV with a dose-rate of 600 MU/min and the gantry was positioned at 0^{o}. Note that the gantry of the linear accelerator rotates around the isocentre to shoot at the tumor from several angles around the patient. The position zero of the gantry is when the beam is vertical above the patient. The effect of fixing a solid water phantom in the beam as well as the effect of the jaws opening was determined while the multileaf collimator (MLC) remained open. Solid water is a polymer

having characteristics very close to those of water. Secondary neutron measurements were carried out on the patient couch at 1 and 2 m from the Linac as well as at the maze-room junction. The purpose of the maze is to reduce the amount of scattered radiation escaping the treatment room (photons or neutrons). All measurements were undertaken at the height of the isocenter and were completed with a total dose of 600 MU per moderator. The current produced was collected by a Supermax electrometer (Standard Imaging Inc, 3120 Deming way, Middleton, WI) and converted to a count-rate using the vendor supplied calibration coefficient of 7.0 fA/(counts/s).

In the case of proton beams, secondary neutron measurements were executed on the patient couch and in the maze-room junction. The effect of the beam energy on the production of secondary neutrons was analyzed by choosing to operate at 2 energies: 60 and 200 MeV while the effect of a phantom along the proton beam was evaluated by using a water tank.

3.7: ICRP neutron weighting factor

We aim to study neutron interactions with biological tissues, for instance the human body. This study consists of determining the secondary species generated by these neutrons and examining the physics underlying the energy dependence of the neutron weighting factor provided by the International Commission on Radiological Protection (ICRP) reports.

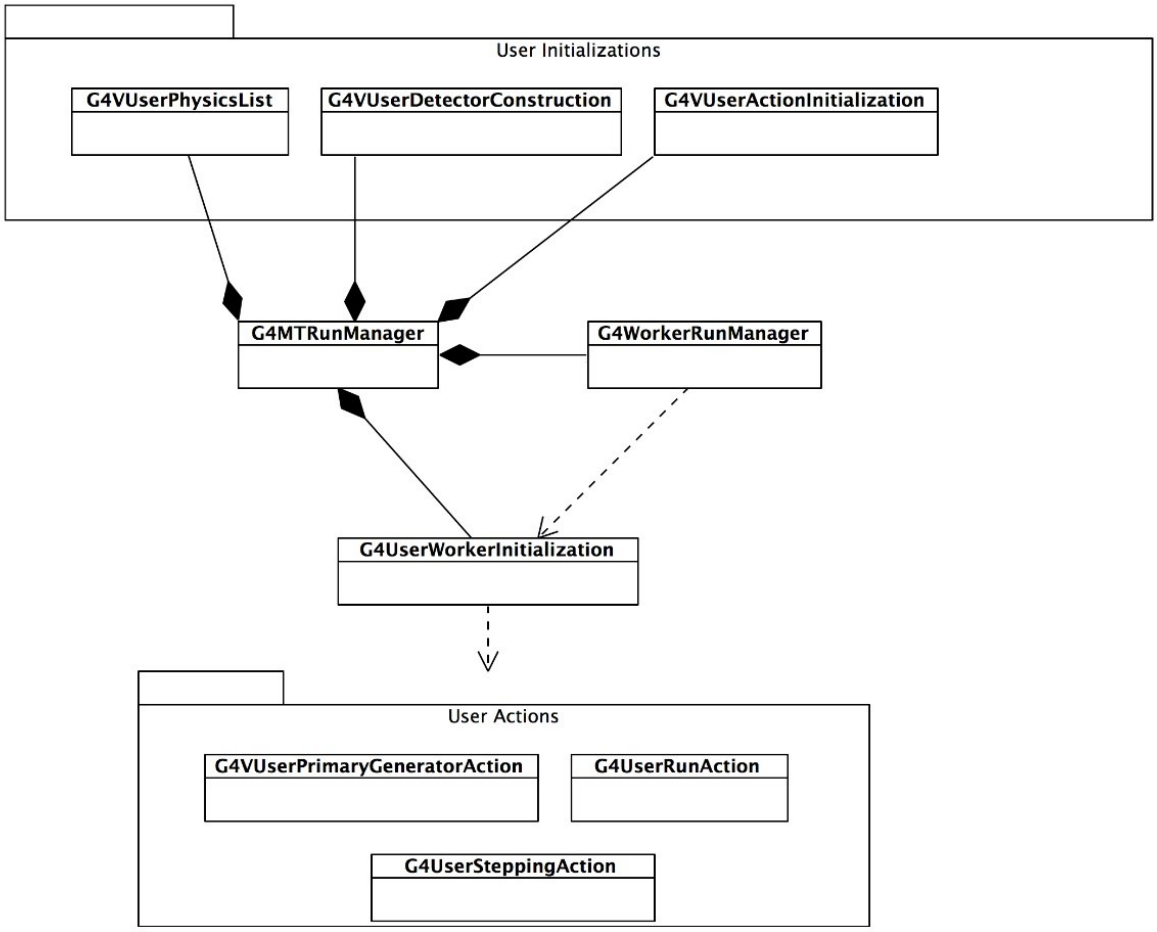

Figure 3.8 Class diagram for main run category classes of the used GEANT4 code.

In order to execute this work, the MC toolkit GEANT4 is used to simulate a monoenergetic neutron beam hitting a water phantom for a range of neutron beam energies. GEANT 4 is a toolkit for simulating the passage of particles through matter. GEANT 4 is used in applications in particle physics, nuclear physics, accelerator design, space engineering and medical physics [23]. More specifically, the Hadr03 example provided by the GEANT4 library was used and modified to match our condition.

GEANT4 was used to compute total cross sections from the direct evaluation of the mean free path, to identify nuclear reactions and to plot energy spectrum of secondary particles. Note that

the total cross section presents the probability of interaction and the mean free path is the average distance traveled by a particle between two successive interactions. The phantom used was a single box representing a homogeneous medium. Two parameters define the geometry that was built in the DetectorConstruction module: 1) the material of the box which is water and 2) the (full) size of the box which is 30 cm^3.

The Primary Generator:

The primary kinematic consists of a single particle starting at the edge of the box. The type of the particle and its energy are set in PrimaryGeneratorAction (For example a neutron with an energy of 1 MeV).

Physics:

An event is killed at the first interaction of the incident particle. The absorption length, also called mean free path, is computed as the mean value of the track length of the incident particle. This is why the medium must be 'infinite': to be sure that an interaction always occurs. The list of nuclear reactions that occurred was printed. Then, the total list of generated particles and ions was obtained. The energy spectrum of the scattered particle and of the created secondary species are plotted.

Histograms:

The code contains 12 built-in 1D histograms, which are managed by G4AnalysisManager and its Messenger.

Chapter 4: Results

4.1: Comparison between MLEM and MAP results

Our first goal in this work is to ensure that we obtained accurate secondary neutron spectra using our detection and unfolding technique (for electron and proton beams).

For this purpose, two unfolding methods (MLEM and MAP) were used and compared with each other. As described earlier, MLEM and MAP are iterative methods, meaning that in order to unfold the data, a certain number of iterations must be executed.

To verify the efficiency of MLEM and MAP to generate secondary neutron spectra around electron and proton beams, both methods were applied first to reproduce a secondary neutron spectrum around an 18 MV photon beam in a bunker housing a Varian Clinac 21EX at the Montreal General Hospital. Note that this spectrum is shown in Fig. 3.5 (a) which was produced previously using MLEM method, validated by Monte Carlo simulation and published by Maglieri et al (2015) [20].

As we notice in Fig. 4.1, both methods give the same secondary neutron spectrum from an 18 MV photon beam for 2800 iterations as used in the Maglieri et al. paper, which gives us confidence that the MAP is a valid unfolding method to produce accurate neutron spectra.

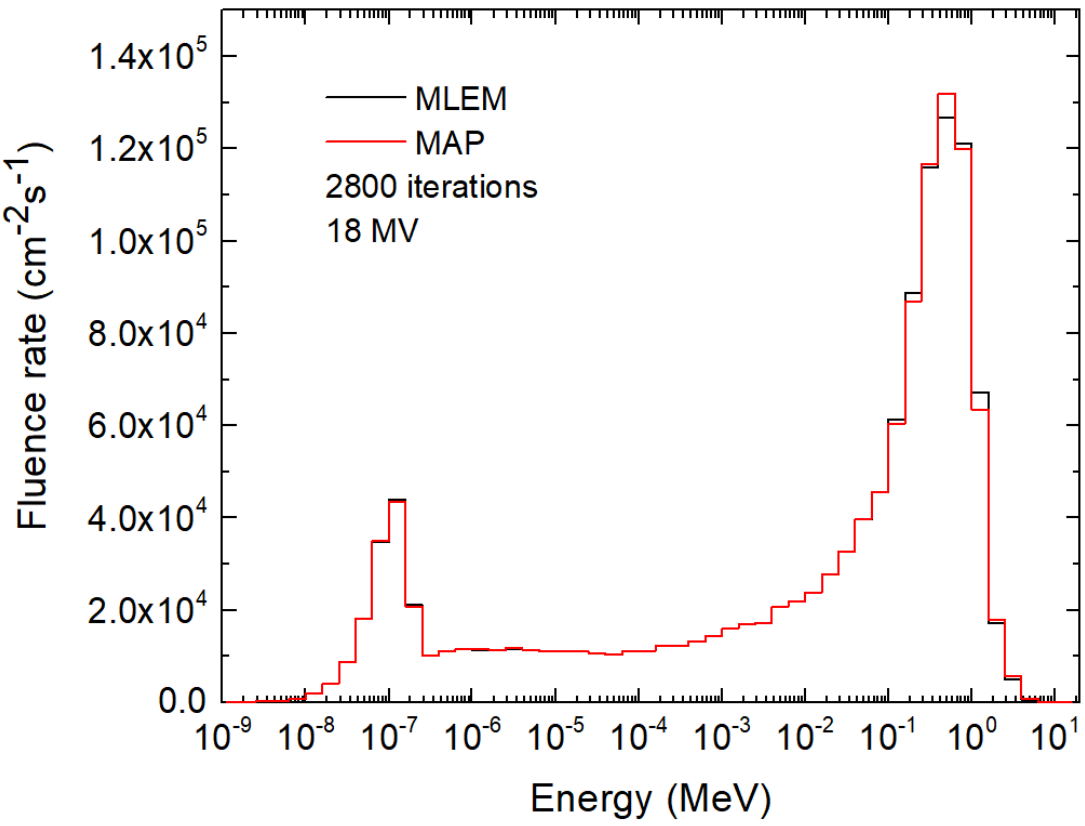

Figure 4.1 Histogram of the secondary neutron fluence rate as a function of neutron energy. The spectrum was unfolded using the MLEM and MAP methods. These secondary neutrons are generated around a 18 MV photon beam.

The next question to be asked is when should we confidentially stop the unfolding algorithm (i.e. after how many iterations) in order to get the most accurate results when Monte Carlo models are not available to validate the results. To answer this important question, we unfolded electron and proton beam data for various conditions using the two methods while increasing each time the number of iterations.

In Fig. 4.2, four secondary neutron spectra are shown. These spectra were unfolded using MLEM algorithm for 2000, 4000, 6000 and 8000 iterations respectively. These spectra correspond to an

electron beam of 20 MeV. Note that the detector was fixed on the couch 1 m away from the isocentre and the jaws were closed with no phantom in the beam path.

As we can see, the fluence rate increases with the number of iterations specially for the thermal and evaporation peaks. For instance, the fluence rate of the evaporation peak increases from 2600 to 3500 $cm^{-2}s^{-1}$ when increasing the number of iterations from 2000 to 8000. This clearly indicates that the number of iterations chosen can affect the calculated fluence rate.

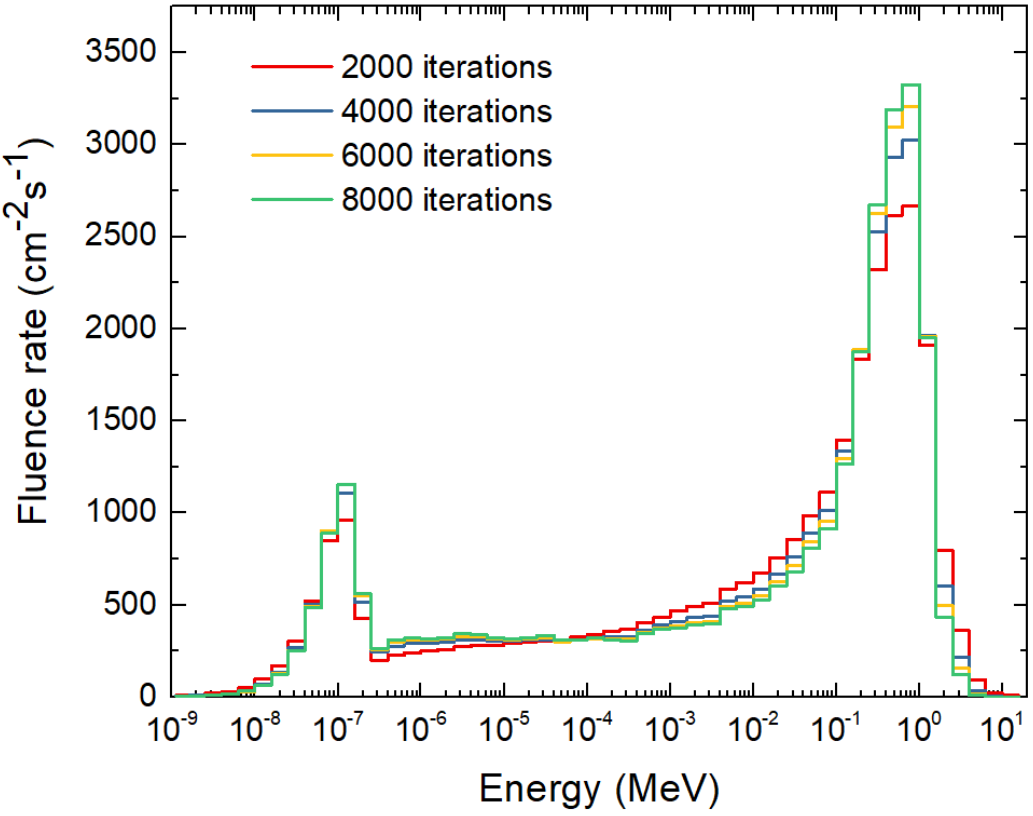

Figure 4.2 Histogram of the secondary neutron fluence rate as a function of neutron energy. The spectrum was unfolded using the MLEM algorithm for 2000, 4000, 6000 and 8000 iterations respectively. These secondary neutrons are generated from an electron beam of 20 MeV, the detector was placed 1 m away from the isocentre and the jaws were closed.

On the other hand, the secondary neutron spectra unfolded by the MAP method for 2000, 4000, 6000 and 8000 iterations respectively are shown in Fig. 4.3. These spectra correspond also to an

electron beam of 20 MeV. The detector was fixed on the couch 1 meter away from the isocentre and the jaws were closed with no phantom in the beam path. As we can clearly see, the neutron spectrum for 2000 iterations differs from the one for 4000 iterations. However, starting from 4000 iterations, the neutron spectra and their corresponding fluence rate values are relatively unchanged when increasing the iteration number from 4000 to 8000. This indicates that for this condition (electron beam of 20 MeV), iterating the data 4000 times makes a good choice at which to stop the iterations in order to get accurate secondary neutron spectra.

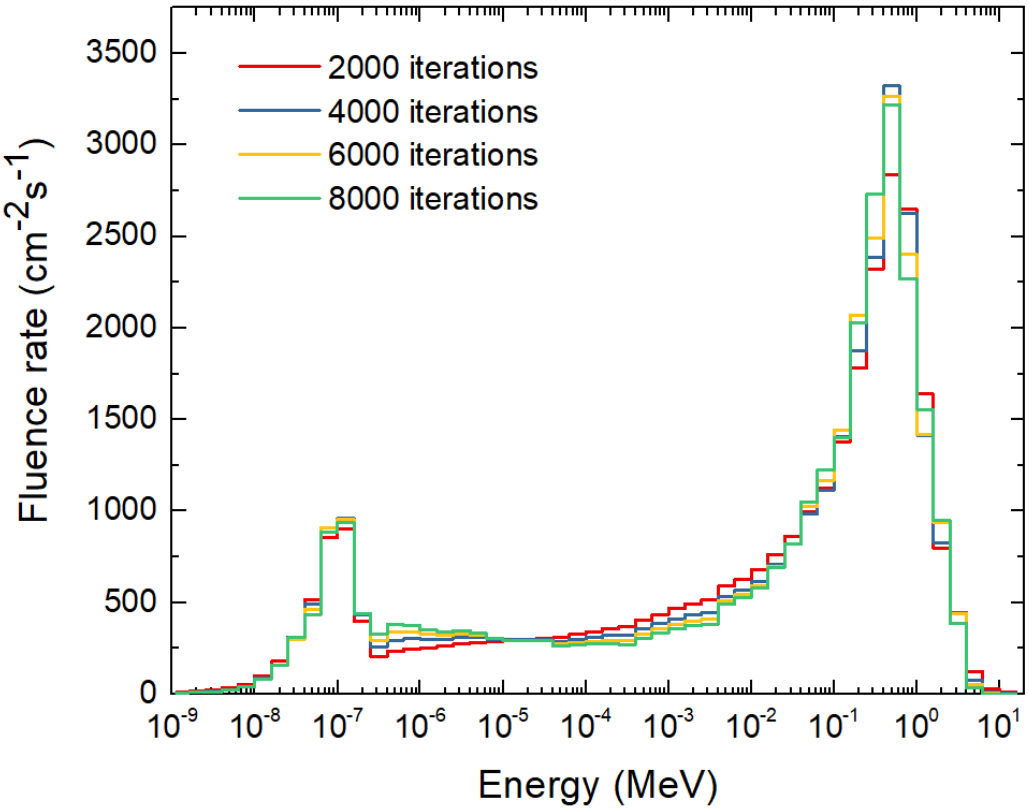

Figure 4.3 Histogram of the secondary neutron fluence rate as a function of neutron energy. The spectrum is unfolded using the MAP algorithm for 2000, 4000, 6000 and 8000 iterations respectively. These secondary neutrons are generated from an electron beam of 20 MeV, the detector was placed 1 m away from the isocentre and the jaws were closed.

In order to go deeper in this investigation, the ambient dose equivalent rate was calculated through the procedure explained in the previous chapter. The variation of the secondary neutron

dose equivalent rate from electron beams (12 and 20 MeV) as a function of the number of iterations for both methods (MLEM and MAP) is shown in Fig. 4.4 and Fig. 4.5 respectively.

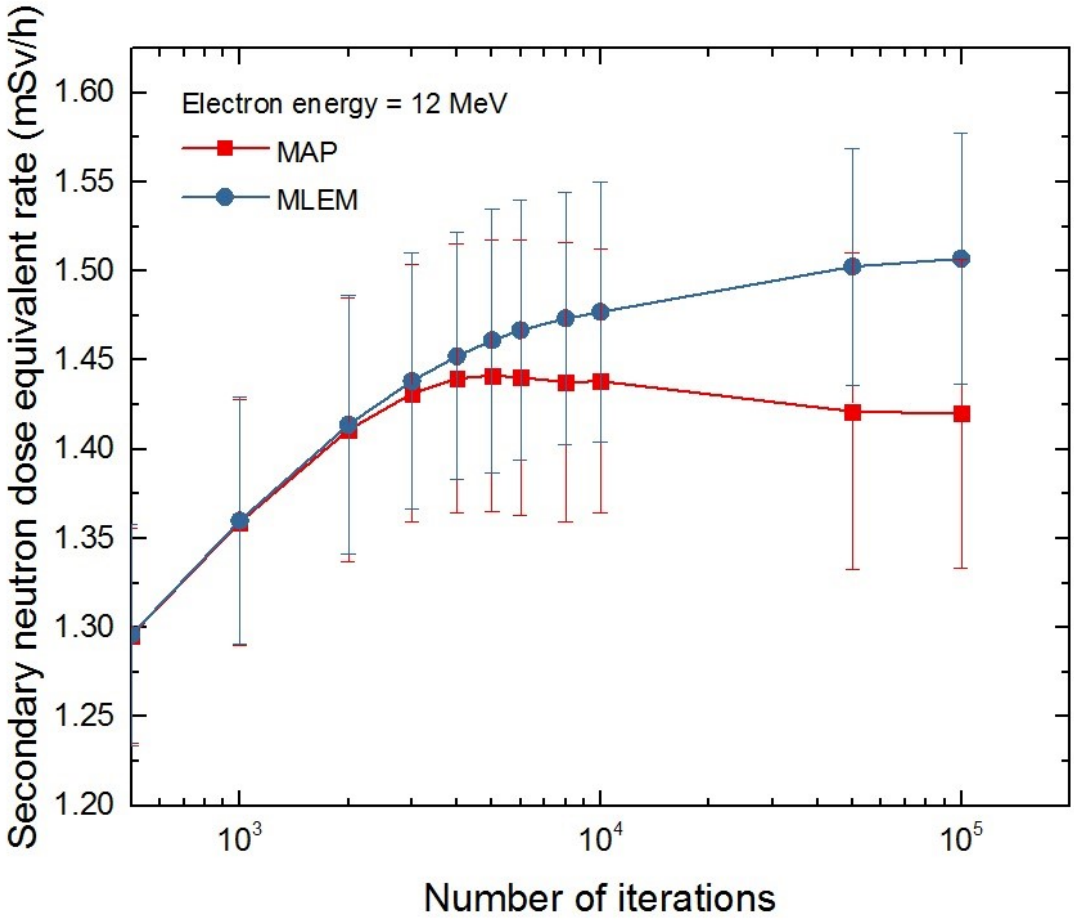

Figure 4.4 Variation of the secondary neutron dose equivalent rate as a function of the number of iterations for both methods (MLEM and MAP). The secondary neutrons are generated from a 12 MeV electron beam, the detector was placed 1 m away from the isocentre and the jaws were closed.

When the electron energy is equal to 12 MeV (Fig. 4.4), we notice that the difference in the values of the secondary neutron dose equivalent rate given by the two methods lies within the uncertainty range, which means that both methods give similar results regardless of the number of iterations. On the other hand, we notice a difference in the behavior of the curves as a function of the number of iterations. In the case of the MLEM method, the neutron dose equivalent rate is an increasing function with the number of iterations while in the case of MAP, the dose

equivalent rate reaches a maximum value around 4000 iterations before reaching a plateau, then starting a slow decrease at a value of 10000 iterations. Note that at an electron energy of 12 MeV, the neutron dose equivalent rate shows low values indicating that electron beams at this energy (12 MeV) generate low number of secondary neutrons in an electron treatment room.

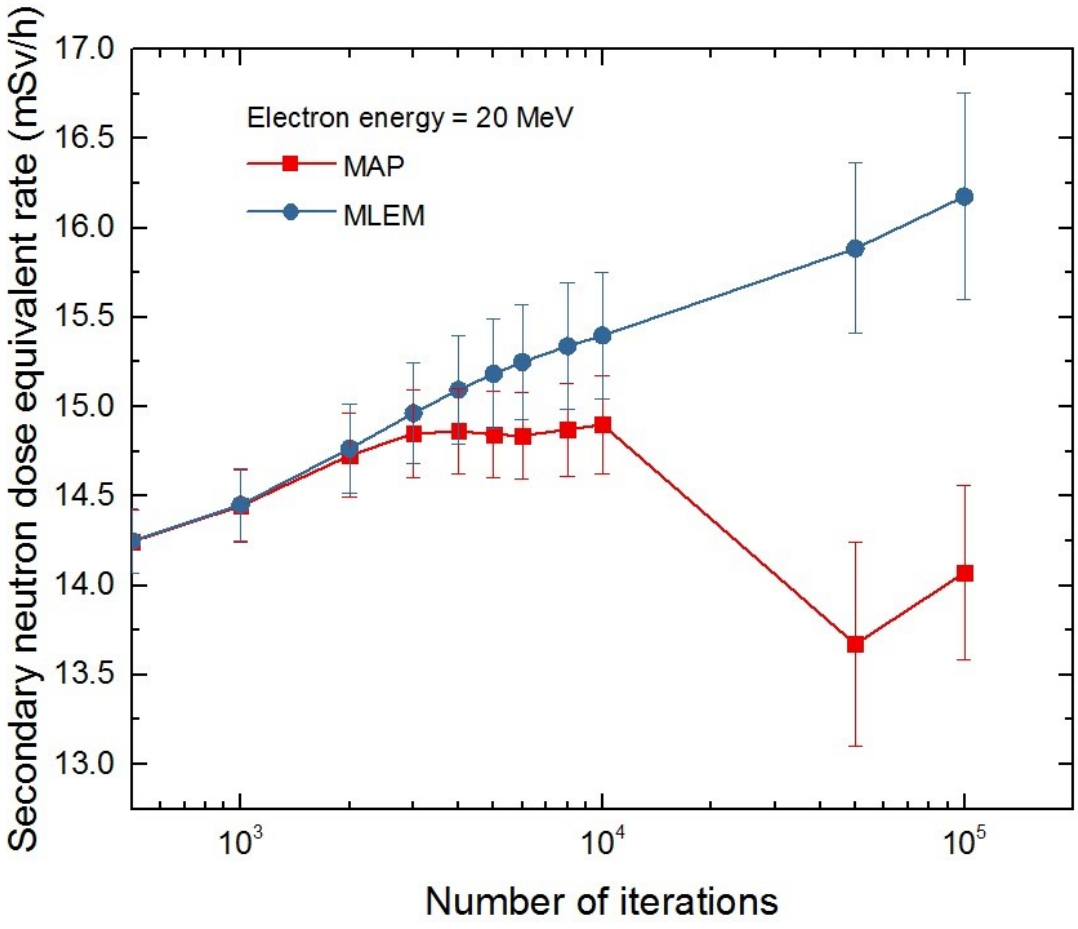

Figure 4.5 Variation of the secondary neutron dose equivalent rate as a function of the number of iterations for both methods (MLEM and MAP). The secondary neutrons are generated from a 20 MeV electron beam, the detector was placed 1 m away from the isocentre and the jaws were closed.

When the electron energy is equal to 20 MeV (Fig. 4.5), we notice that below 10000 iterations, both methods (MLEM and MAP) give the same values of secondary neutron dose equivalent rate, within statistical uncertainties, while they give different values above this number of

iterations. On the other hand, we notice a different behavior of the curves as a function of the number of iterations. In the case of the MLEM method, the neutron dose equivalent rate displays a linear increase with the number of iterations while in the case of the MAP method, the dose equivalent rate reaches a maximum value around 4000 iterations before reaching a plateau, then starting a fast decrease at a value of 10000 iterations.

From what is previously shown, one can say that unfolding the measured data by iterating between 3000 and 10000 times gives accurate results for two reasons. First, the secondary neutron dose equivalent rate shows a plateau between 4000 and 10000 iterations when using the MAP method (around 14.8 mSv/h). Second, both methods (MLEM and MAP) give similar values of the secondary neutron dose equivalent rates when iterating between 4000 and 10000 times (Fig. 4.4 and 4.5).

Note that the comparison between the two unfolding methods is performed for every condition of both beams (electron and proton beams) to provide confidence in the number chosen at which to stop the code.

In what follows, MAP method is used to unfold the secondary neutron spectra and to evaluate their risk (dose equivalent rate) with a number of iterations lying in the plateau region.

4.2: Secondary neutrons around clinical electron beams

In this section, the effects of several parameters such as electron energy, field size, presence of a phantom and location in the treatment room on the generation of secondary neutrons around clinical electron beams are determined.

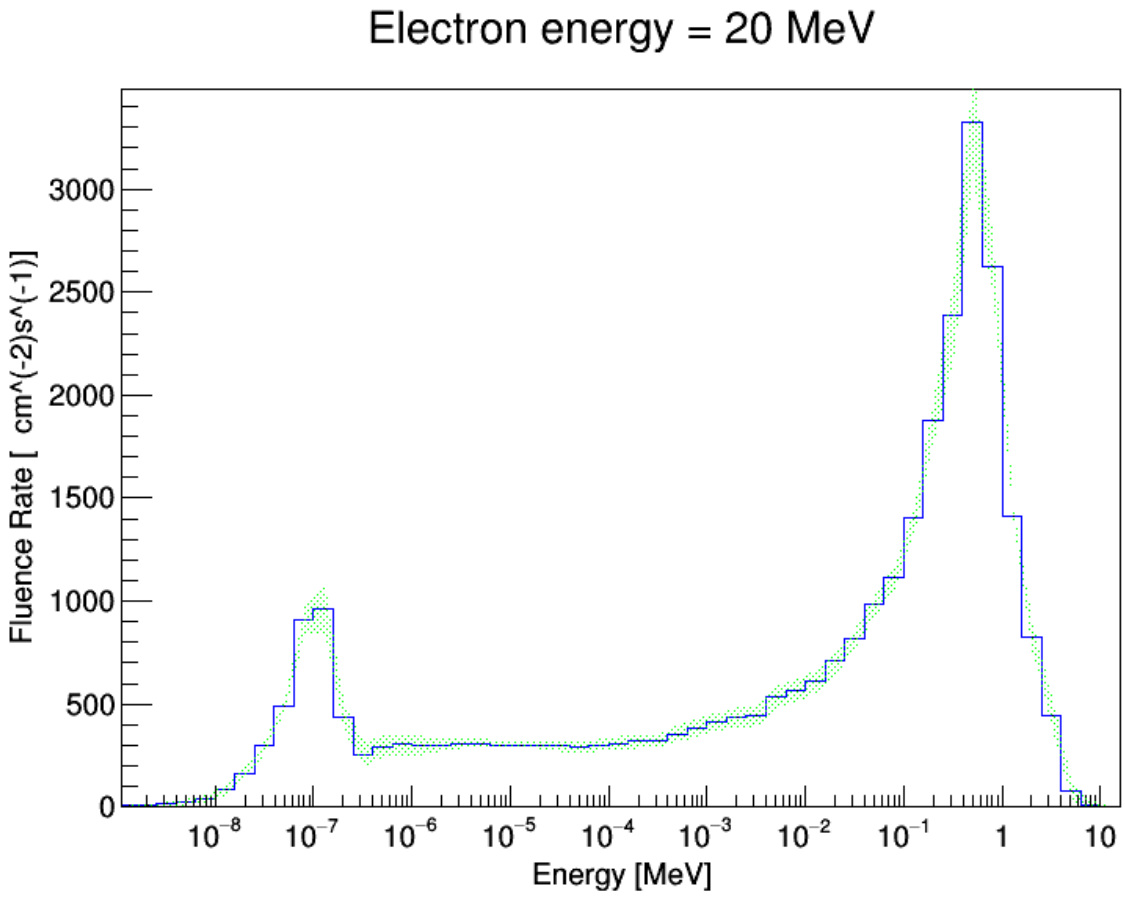

Figure 4.6 Spectrum of secondary neutron fluence rate as a function of neutron energy around a clinical electron beam. The energy of the electron beam being equal to 20 MeV, the neutron detector being fixed 1 m from the isocentre and the jaws being closed with no phantom along the beam path.

In Fig. 4.6, an example of a spectrum of the secondary neutron fluence rate as a function of the neutron energy around a clinical electron beam is shown. This spectrum corresponds to an electron beam energy of 20 MeV where the detector was fixed on the couch 1 meter away from the isocentre and the jaws were closed with no phantom along the beam path. Note that the

spectrum in Fig. 4.6 is represented by the blue line while the uncertainty around it is represented by the green range.

We notice from Fig. 4.6 that the secondary neutrons generated around an electron beam in our treatment room consist of a peak around an energy of 1 MeV due to evaporation processes, and a thermal peak due to neutrons that have scattered around the room before reaching the measurement location. Neutrons also exist between these two peaks in the form of an intermediate energy continuum.

4.2.1: Effect of the beam energy

The effect of the beam energy on the secondary neutron generation around electron beams was studied by modifying the beam energy and by fixing the other parameters: the detector being fixed on the couch 1 meter away from the isocentre, the jaws being closed with no phantom along the beam path. The three spectra of the secondary neutron fluence rate as a function of neutron energy for an electron energy of 12, 16 and 20 MeV respectively are shown in Fig. 4.7.

For an electron energy equal to 12 MeV, low evaporation and thermal peaks are observed with a negligible intermediate energy continuum: the evaporation peak reaching a maximum value of fluence rate around 750 $cm^{-2}s^{-1}$ while the thermal peak reaching a maximum value around 250 $cm^{-2}s^{-1}$.

For an electron energy of 16 and 20 MeV, we observe important evaporation and thermal peaks with an intermediate energy continuum in between: the evaporation peak reaching a maximum value of fluence rate around 3300 $cm^{-2}s^{-1}$ while the thermal peak reaches a maximum value around 1200 $cm^{-2}s^{-1}$. Note that the evaporation and thermal peaks are slightly higher for an

electron energy of 16 MeV while the intermediate energy continuum is slightly higher for an electron energy of 20 MeV.

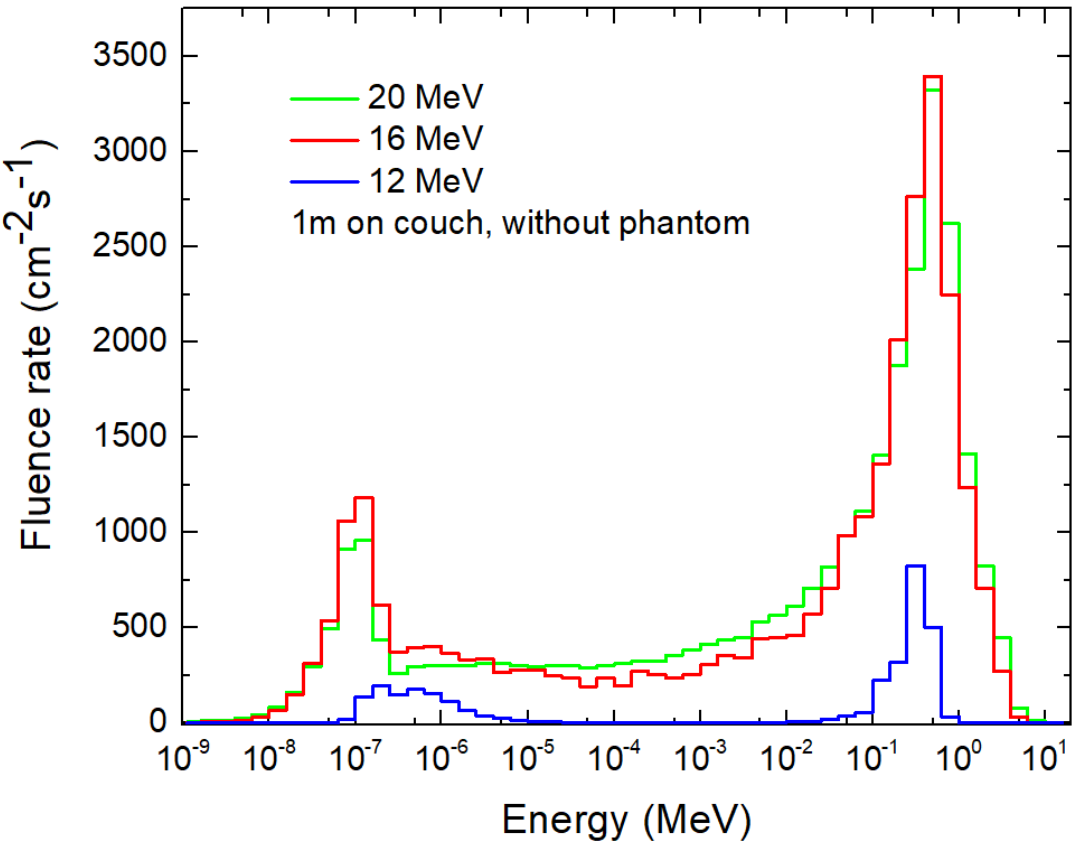

Figure 4.7 Spectra of secondary neutron fluence rate as a function of neutron energy for three electron beam energies: 12, 16 and 20 MeV. The neutron detector being fixed 1 m far from the isocentre and the jaws being closed with no phantom along the beam path.

In addition, the ambient dose equivalent rate is evaluated for the three spectra shown in Fig. 4.7 in order to estimate the risk for stochastic effects associated with the secondary generated neutrons from electron beams with various energies. The results are shown in Table 1.

Electron energy (MeV)	12	16	20
Ambient dose equivalent rate (mSv/h)	1.44 ± 0.08	13.9 ± 0.2	14.9 ± 0.2

Table 1 The secondary neutron ambient dose equivalent rates for various electron energy.

The results shown in Table 1 demonstrate that the ambient dose equivalent rate of the secondary neutrons increases when increasing the electron beam energy. Note that higher energy electron beams are used clinically to treat deeper tumors (for instance, 20 MeV electron beams can be used to treat 4 or 5 cm deep tumors). At the same conditions (1 m from the isocentre and closed jaws), the secondary neutron ambient dose equivalent rate is equal to 10 mSv/h around a photon beam of 10 MV while it is equal to around 360 mSv/h around a 18 MV photon beam. This clearly indicates that the production of secondary neutrons around clinical photon beams is 10 to 20 times higher than the production of these neutrons around clinical electron beams.

4.2.2: Effect of the field size (effect of jaws)

The effect of the field size of the electron beam on the secondary neutron generation is studied by modifying the jaws opening and by fixing the other parameters: the detector being fixed on the couch 1 meter away from the isocentre, the electron energy is fixed at 20 MeV with no phantom along the beam path. The two spectra of the secondary neutron fluence rate as a function of neutron energy for two conditions (jaws open and jaws closed) are shown in Fig. 4.8.

As we notice from Fig. 4.8, the spectra of the secondary neutron fluence rate as a function of the neutron energy differs when the jaws opening is changed. The evaporation and thermal peaks show higher values when the jaws are open while the intermediate energy continuum is clearly higher when the jaws are closed.

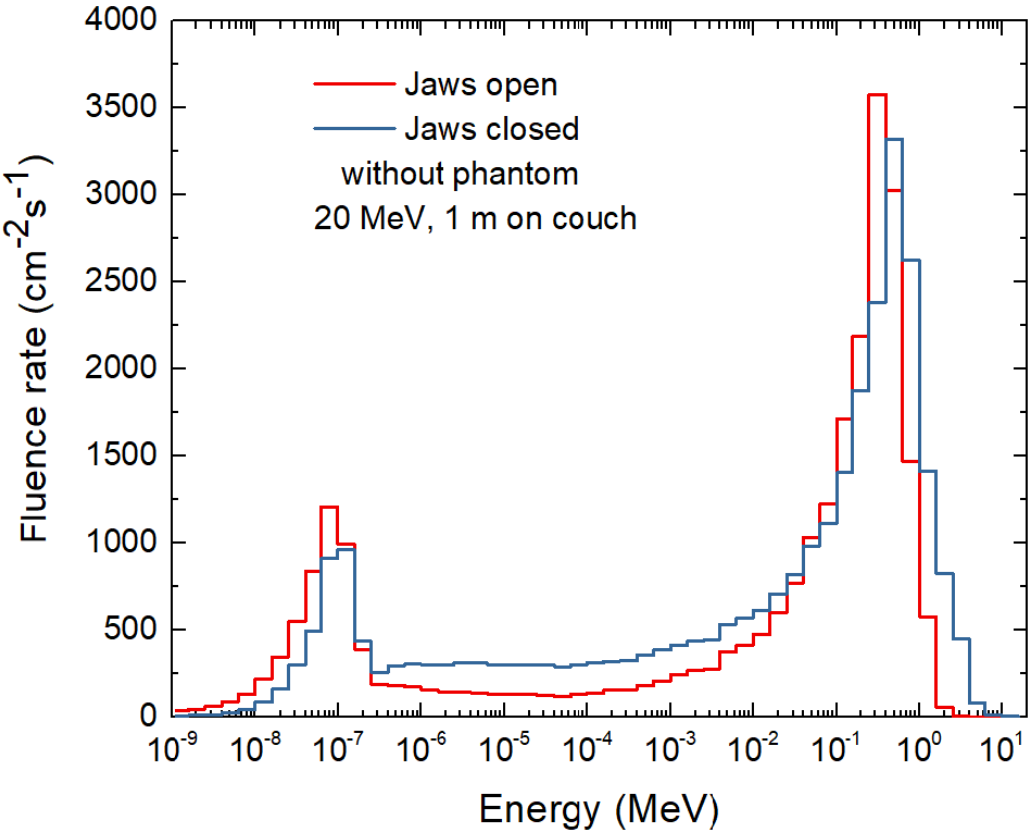

Figure 4.8 Spectra of secondary neutron fluence rate as a function of neutron energy for two different jaws opening. The neutron detector being fixed 1 m far from the isocentre and the electron energy being equal to 20 MeV with no phantom along the beam path.

In addition, the ambient dose equivalent rate is evaluated for both spectra shown in Fig. 4.8 in order to estimate the risk associated to the secondary generated neutrons from electron beams with various jaws opening. The results are shown in Table 2.

Jaws opening	Open	Closed
Ambient dose equivalent rate (mSv/h)	10.9 ± 0.2	14.9 ± 0.2

Table 2 The secondary neutron ambient dose equivalent rates for various jaw openings.

The results shown in Table 2 demonstrate that the ambient dose equivalent rate of the secondary neutrons is higher when the jaws are closed. This clearly indicates that an important generation of secondary neutrons around clinical electron beams does happen in the linac treatment head specially in the collimation system.

4.2.3: Effect of the presence of a phantom

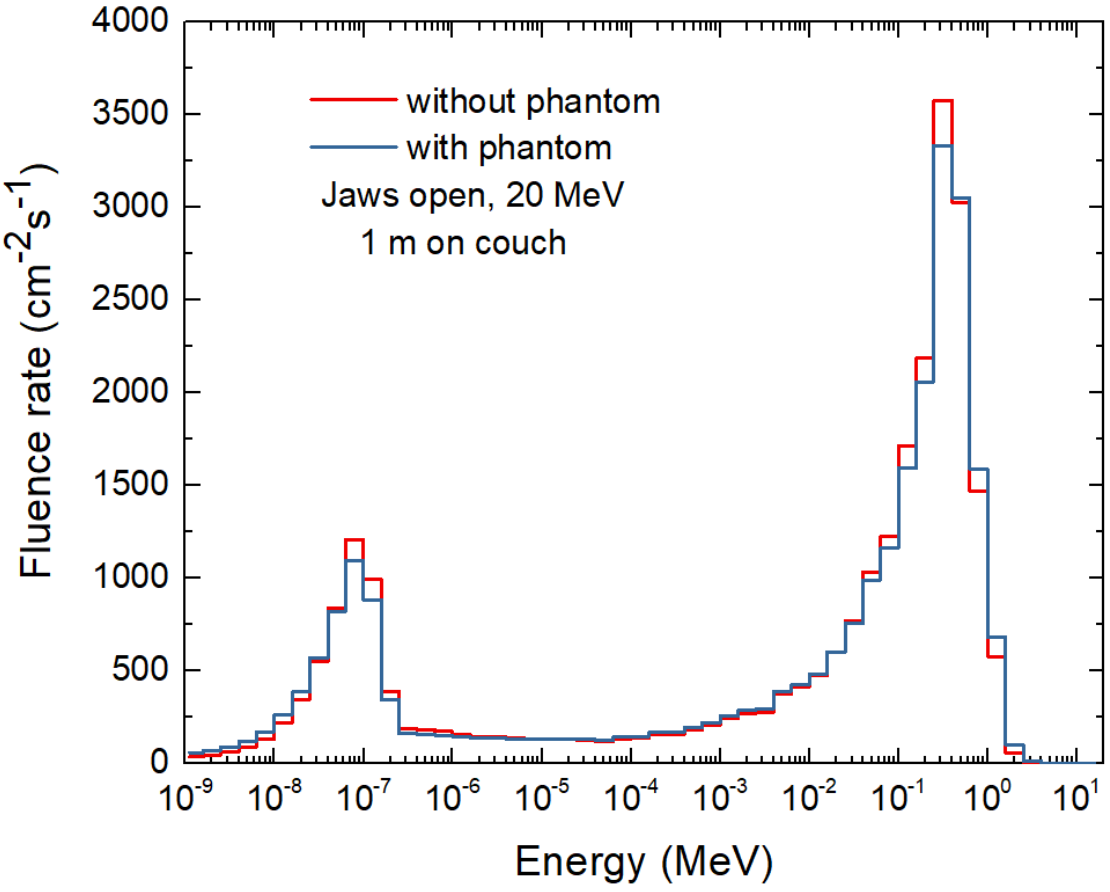

Figure 4.9 Spectra of secondary neutron fluence rate as a function of neutron energy for two different conditions (with and without a solid water phantom). The neutron detector being fixed 1 m far from the isocentre and the electron energy being equal to 20 MeV.

The effect of the presence of a phantom on the secondary neutron generation is studied by putting a solid water phantom within the beam path and by fixing the other parameters: the detector being fixed on the couch 1 meter away from the isocentre, the electron energy is fixed at 20 MeV. Note that the solid water phantom, which has a cubic shape and a volume of around 30 cm^3, covers entirely the field size of the electron beam. The spectra of the secondary neutron fluence rate as a function of neutron energy for two conditions (with and without a solid water phantom) are shown in Fig. 4.9.

As we notice from Fig. 4.9, the spectra of the secondary neutron fluence rate as a function of the neutron energy show a similar behavior with and without the presence of a solid water phantom. The evaporation and thermal peaks show very close values while the intermediate energy continuum is clearly similar for both conditions.

In addition, the ambient dose equivalent rate is evaluated for both spectra shown in Fig. 4.9 in order to estimate the risk associated with the secondary generated neutrons from electron beams with and without the presence of a solid water phantom along the beam path. The results are shown in Table 3.

Solid water phantom	With	Without
Ambient dose equivalent rate (mSv/h)	11 ± 0.2	10.9 ± 0.2

Table 3 The secondary neutron ambient dose equivalent rates with and without solid water phantom.

The results shown in Table 3 demonstrate that the ambient dose equivalent rate of the secondary neutrons is similar with and without the presence of a solid water phantom along the electron beam path.

4.2.4: Effect of the location in the treatment room

The effect of the location in the treatment room on the secondary neutron fluence rates around electron beams is studied by modifying the detector position and by fixing the other parameters: the electron beam energy is fixed at 20 MeV, the jaws are open and no phantom is fixed in the beam path. The three spectra of the secondary neutron fluence rate as a function of neutron energy for three measurement positions (on the couch 1 meter and 2 meters away from the isocentre and in the maze-room junction) are shown in Fig. 4.10.

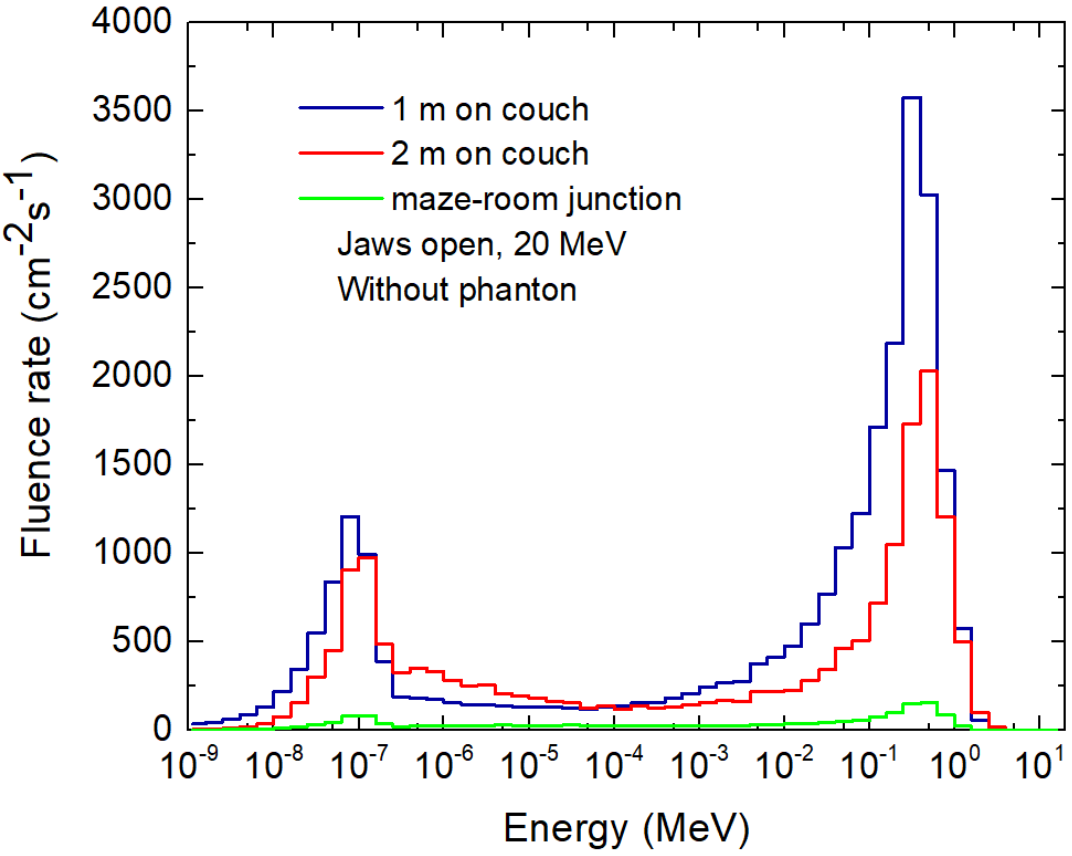

Figure 4.10 Spectra of secondary neutron fluence rate as a function of neutron energy for three measurement positions: on the couch 1 meter and 2 meters away from the isocentre and in the maze-room junction. The electron beam energy being fixed at 20 MeV with no phantom along the electron beam.

As we notice from the three spectra shown in Fig. 4.10, the secondary neutron fluence rate values are higher when the measurement taken is closer to the treatment beam over the whole range of neutron energies. For instance, the thermal peak reaches a maximum value of fluence rate of around 100 $cm^{-2}s^{-1}$ in the maze-room junction while it reaches around 1000 and 1250 $cm^{-2}s^{-1}$ on the couch 2 meters and 1 meter away from the isocentre respectively. The evaporation peak reaches a maximum value of around 200 $cm^{-2}s^{-1}$ in the maze-room junction while it reaches around 2000 and 3500 $cm^{-2}s^{-1}$ on the couch 2 meters and 1 meter away from the isocentre respectively.

The ambient dose equivalent rate is evaluated for the three spectra shown in Fig. 4.10 in order to estimate the risk associated to the secondary generated neutrons from electron beams at different locations in the treatment room. The results are shown in Table 4.

Location in the treatment room	1 m on couch	2 m on couch	Maze-room junction
Ambient dose equivalent rate (mSv/h)	10.92 ± 0.21	7.03 ± 0.19	0.54 ± 0.05

Table 4 The secondary neutron ambient dose equivalent rates for various locations in the treatment room.

The results shown in Table 4 demonstrate that the ambient dose equivalent rate of the secondary neutrons decreases when the distance between the treatment beam and the measurement increases. This is due to the attenuation and absorption of the secondary neutrons generated around an electron beam as they travel in the treatment room.

4.3: Secondary neutrons around clinical proton beams

As in the previous section, the effects of several parameters such as proton energy, presence of a phantom and location in the treatment room on the generation of secondary neutrons around clinical proton beams are determined in this section.

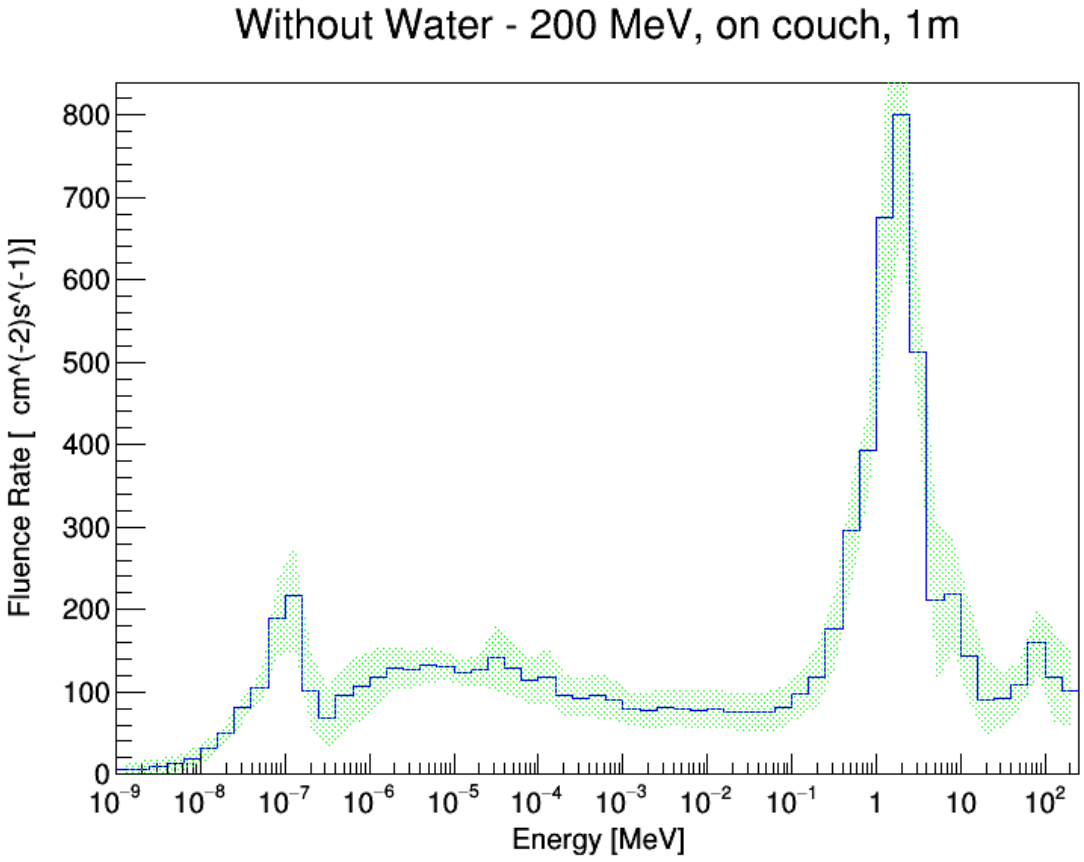

Figure 4.11 Spectra of secondary neutron fluence rate as a function of neutron energy around a clinical proton beam. The energy of the proton beam being equal to 200 MeV, the neutron detector being fixed 1 m far from the isocentre with no phantom along the beam path.

In Fig. 4.11, an example of a spectrum of the secondary neutron fluence rate as a function of the neutron energy around a clinical proton beam is shown. This spectrum corresponds to a proton energy of 200 MeV where the detector being fixed on the couch 1 meter away from the isocentre

with no phantom along the beam path. Note that the spectrum in the Fig. 4.11 is represented by the blue line while the uncertainty around it is represented by the green range.

We notice from Fig. 4.11 that the secondary neutrons generated around a proton beam in the treatment room have a wide energy range, from thermal up to the maximum beam energy which is equal to 200 MeV. This secondary neutron spectrum has three pronounced peaks. The first peak comprises direct neutrons and lies around 200 MeV. The second peak is due to evaporation processes and ranges from approximately 100 keV to approximately 10 MeV. The third is a thermal peak due to neutrons that have scattered around the room and returned to the measurement location. Neutrons also exist between these peaks in the form of an intermediate energy continuum.

4.3.1: Effect of the beam energy

The effect of the beam energy on the secondary neutron generation around proton beams is studied by modifying the beam energy and by fixing the other parameters: the detector being fixed on the couch 1 meter away from the isocentre and no phantom being fixed along the beam path. The two spectra of the secondary neutron fluence rate as a function of neutron energy for a proton energy of 60 and 200 MeV respectively are shown in Fig. 4.12.

The difference between the two spectra is that the secondary neutron fluence rate values are much higher for a proton energy of 200 MeV than for 60 MeV over the whole range of neutron energies. For instance, the thermal peak reaches a maximum value of fluence rate of around 4 $cm^{-2}s^{-1}$ for a proton energy of 60 MeV while it reaches around 250 $cm^{-2}s^{-1}$ for 200 MeV. In addition, the evaporation peak reaches a maximum value of around 30 $cm^{-2}s^{-1}$ for a proton energy of 60 MeV while it reaches around 1000 $cm^{-2}s^{-1}$ for 200 MeV.

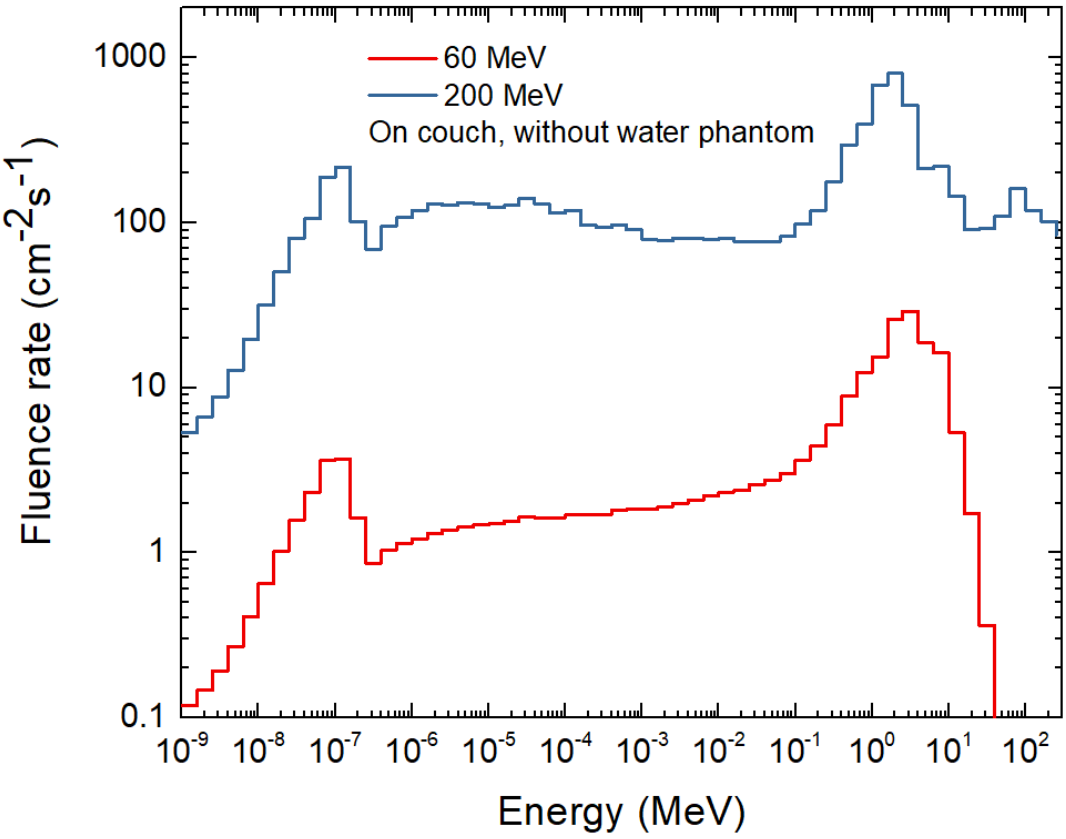

Figure 4.12 Spectra of secondary neutron fluence rate as a function of neutron energy for two proton beam energies: 60 and 200 MeV. The neutron detector being fixed 1 m far from the isocentre with no phantom along the beam path.

Then, the ambient dose equivalent rate is evaluated for both spectra shown in Fig. 4.12 in order to estimate the risk associated to the secondary generated neutrons from proton beams with various energies. The results are shown in Table 5.

Proton energy (MeV)	60	200
Ambient dose equivalent rate (mSv/h)	0.21 ± 0.03	6.1 ± 0.1

Table 5 The secondary neutron ambient dose equivalent rates for various proton energies.

The results shown in Table 5 demonstrate that the ambient dose equivalent rate of the secondary neutrons clearly increases when augmenting the proton beam energy.

4.3.2: Effect of the presence of a phantom

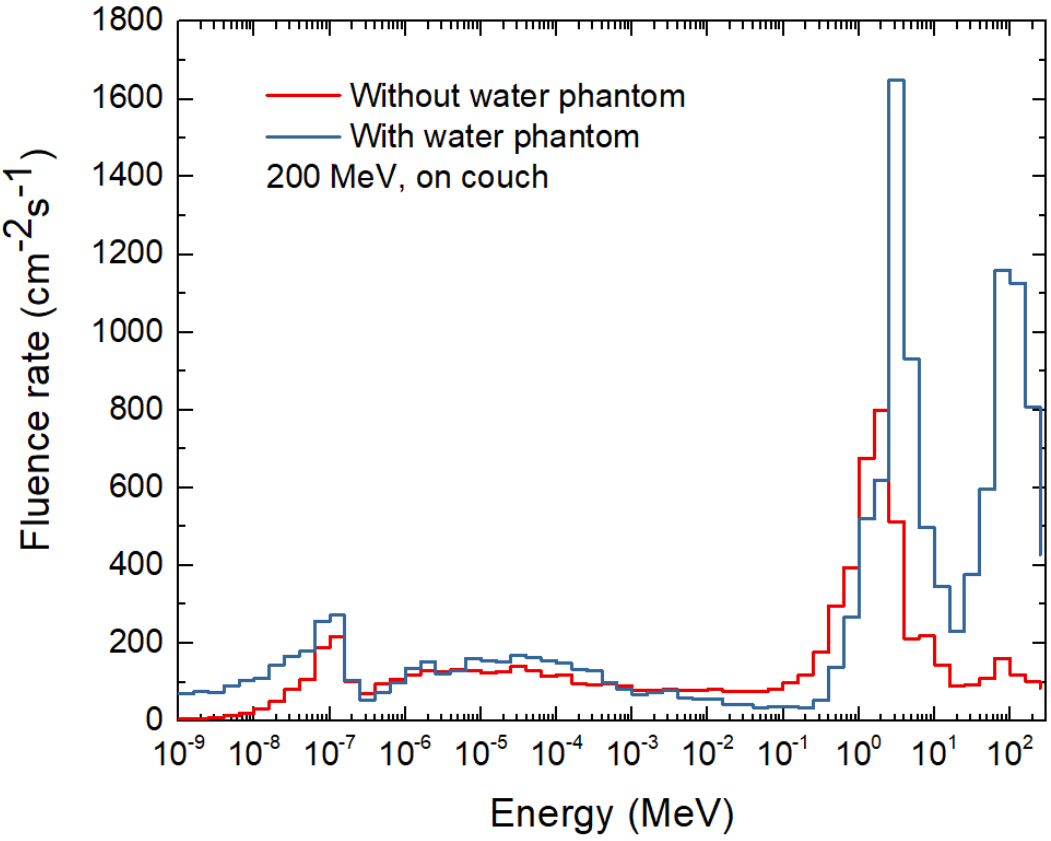

Figure 4.13 Spectra of secondary neutron fluence rate as a function of neutron energy for two different conditions (with and without a water phantom). The neutron detector being fixed 1 m far from the isocentre and the proton energy being equal to 200 MeV.

The effect of the presence of a phantom on the secondary neutron generation was studied by putting a water phantom within the beam path and by fixing the other parameters: the detector being fixed on the couch 1 meter away from the isocentre and the proton energy is fixed on 200 MeV. The two spectra of the secondary neutron fluence rate as a function of neutron energy for two conditions (with and without a water phantom) are shown in Fig. 4.13.

When adding a water phantom along the proton beam path, we notice from Fig. 4.13 that:

1) The thermal peak and the intermediate energy continuum do not change significantly.
2) The evaporation and the direct peaks increase significantly. For instance, the evaporation peak increases from 800 to 1600 $cm^{-2}s^{-1}$ and the direct peak increases from 150 to 1150 $cm^{-2}s^{-1}$.

In addition, the ambient dose equivalent rate is evaluated for both spectra shown in Fig. 4.13 in order to estimate the risk associated with the secondary generated neutrons from proton beams with and without the presence of a water phantom along the beam path. The results are shown in Table 6.

Water phantom	With	Without
Ambient dose equivalent rate (mSv/h)	13.4 ± 0.2	6.1 ± 0.1

Table 6 The secondary neutron ambient dose equivalent rates with and without water phantom.

The results shown in Table 6 demonstrate that the ambient dose equivalent rate of the secondary neutrons is higher with the presence of a water phantom in the path of the proton beam. This clearly indicates that an important generation of secondary neutrons around clinical proton beams does happen in the water phantom which means a high proportion of secondary neutrons generated in the patient body.

4.3.3: Effect of the location in the treatment room

The effect of the location in the treatment room on the secondary neutron detection around proton beams was studied by modifying the detector position and by fixing the other parameters: the proton beam energy is fixed at 200 MeV with a water phantom in the beam path. The two

spectra of the secondary neutron fluence rate as a function of neutron energy for two measurement positions (on the couch 1 meter away from the isocentre and in the maze-room junction) are shown in Fig. 4.14.

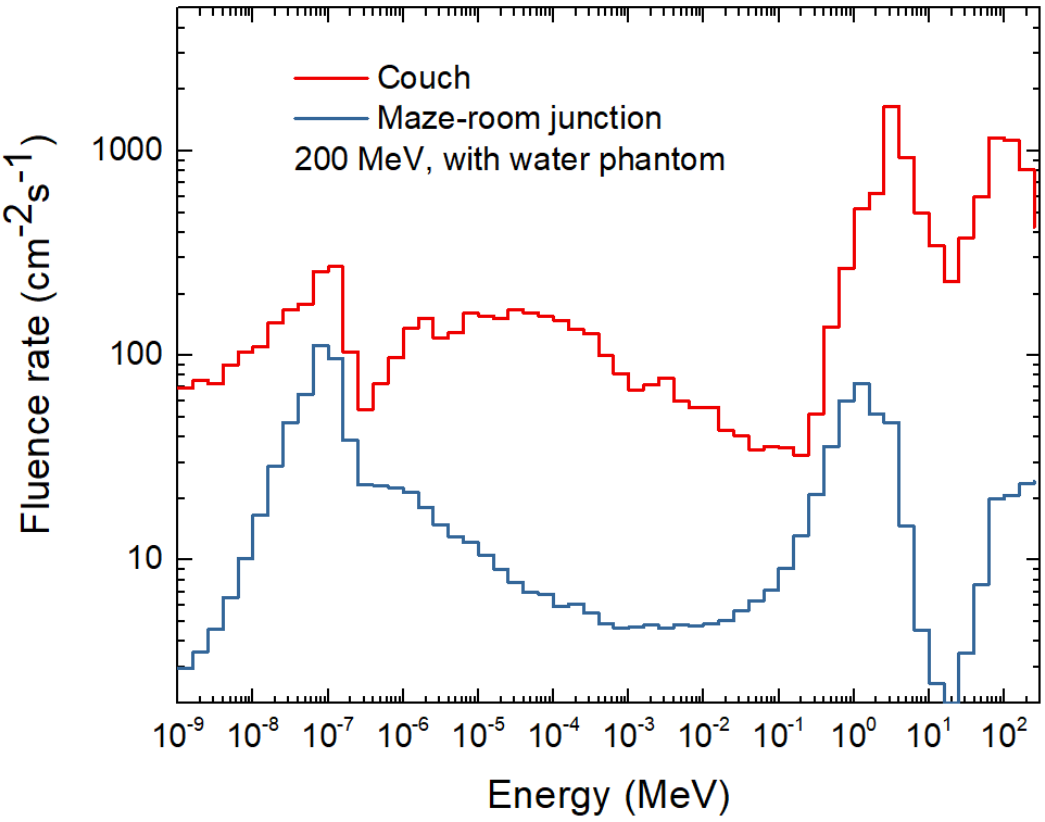

Figure 4.14 Spectra of secondary neutron fluence rate as a function of neutron energy for two measurement positions: on the couch 1 meter away from the isocentre and in the maze-room junction. The proton beam energy being fixed at 200 MeV with a water phantom along the proton beam.

As we notice from the two spectra shown in Fig. 4.14, the secondary neutron fluence rate values are higher on the couch than in the maze-room junction over the whole range of neutron energies. For instance, the thermal peak reaches a maximum value of fluence rate of around 100 $cm^{-2}s^{-1}$ in the maze-room junction while it reaches around 300 $cm^{-2}s^{-1}$ on the couch. The evaporation peak reaches a maximum value of around 75 $cm^{-2}s^{-1}$ in the maze-room junction

while it reaches around 2000 $cm^{-2}s^{-1}$ on the couch. The direct peak reaches a maximum value of around 25 $cm^{-2}s^{-1}$ in the maze-room junction while it reaches around 1000 $cm^{-2}s^{-1}$ on the couch. The second difference between the two spectra lies in the fact that the thermal peak is the lowest one in the spectrum corresponding to the measurement done on the couch while it is the highest peak in the spectrum corresponding to the maze-room junction measurement. This is due to the thermalizing of the secondary neutrons by scattering in the treatment room.

The ambient dose equivalent rate is evaluated for both spectra shown in Fig. 4.14 in order to estimate the risk associated with the secondary generated neutrons from proton beams at different locations in the treatment room. The results are shown in Table 7.

Location	Couch	Maze-room junction
Ambient dose equivalent rate (mSv/h)	13.4 ± 0.2	0.57 ± 0.05

Table 7 The secondary neutron ambient dose equivalent rates for various locations in the treatment room.

The results shown in Table 7 demonstrate that the ambient dose equivalent rate of the secondary neutrons is higher on the treatment couch than in the maze-room junction. This is due to the attenuation and absorption of the secondary neutrons generated around a proton beam as they travel in the treatment room.

4.4: Neutron track structure

In Fig. 4.15, an example of an energy spectrum produced by the GEANT4 code is shown. This spectrum corresponds to secondary protons generated in a water phantom by a monoenergetic neutron beam of 1000 neutrons having an energy of 1 MeV. As expected, the maximum energy attained by these secondary protons matches exactly the energy of the monoenergetic incident neutron beam.

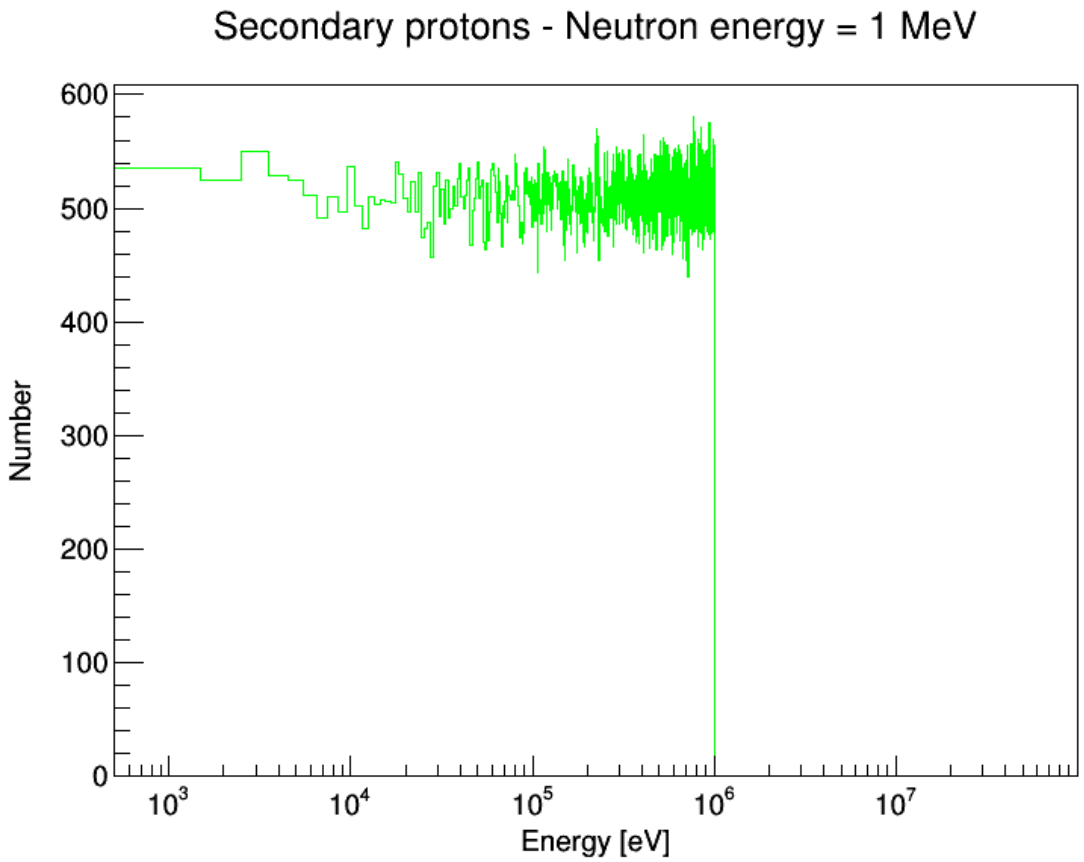

Figure 4.15 Histogram of secondary protons generated in a water phantom by a monoenergetic neutron beam consisting of 1000 neutrons with an energy of 1 MeV.

4.4.1: Generated particles in a phantom by a monoenergetic neutron beam

The variation of neutron interaction type in the water phantom and the variation of the generated particle number as a function of the incident neutron beam energy are shown in Fig 4.16 and 4.17 respectively. Note that the initial number of neutrons in the incident beam interacting with the water phantom is set to 1×10^6.

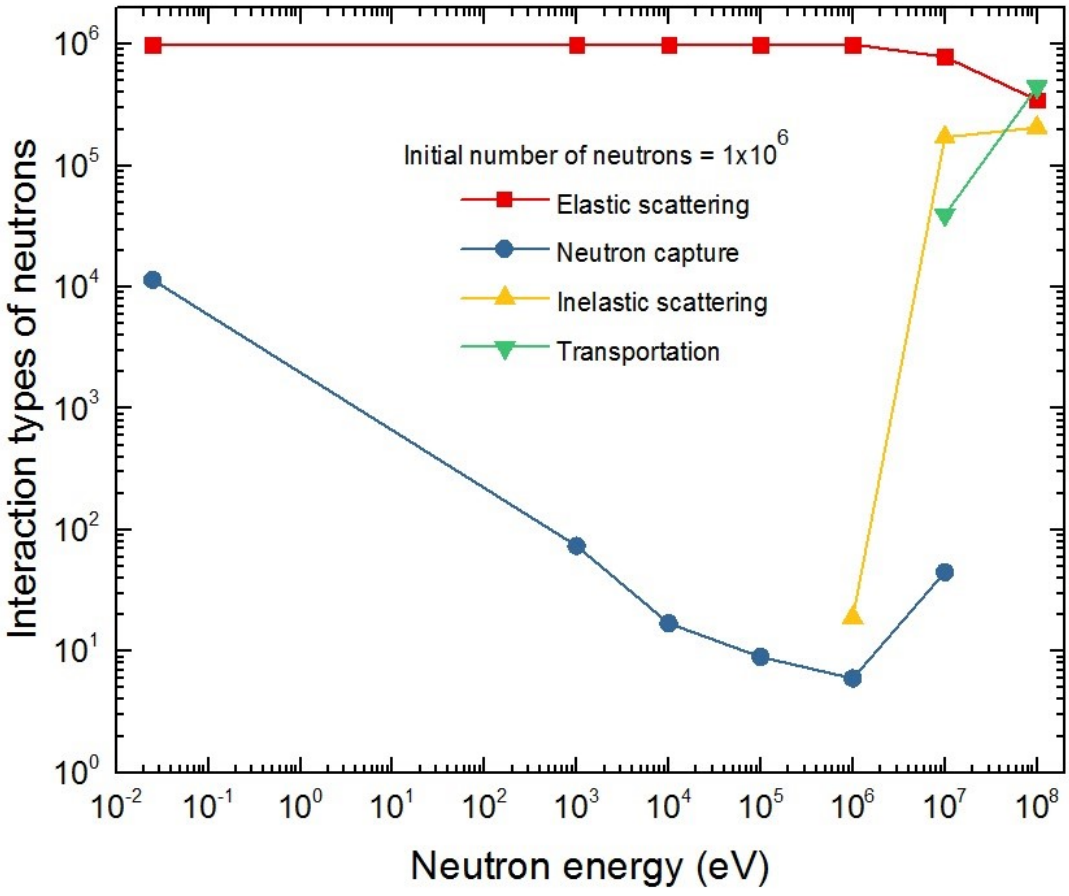

Figure 4.16 Variation of neutron interaction type in a water phantom as a function of the incident neutron beam energy. Note that the initial number of neutrons in the incident beam interacting with the water phantom is set to 1×10^6.

As shown in Fig. 4.16, the main neutron interaction in the water phantom is elastic scattering. As the neutron energy increases from 0.01 eV to 1 MeV, it keeps a constant value of around 1×10^6 while it starts a decrease for a neutron energy above 1 MeV.

The neutron capture interaction is also important. The frequency of this interaction decreases when the neutron energy augments reaching a minimum value for a neutron energy of 1 MeV. Then, it starts to increase for a neutron energy above 1 MeV.

The inelastic scattering of incident neutrons in the water phantom starts to appear for a neutron energy of around 1 MeV. It shows a fast increase below a neutron energy of 10 MeV and a slow increase above this energy.

In addition, above a neutron energy of 10 MeV, the probability of transportation becomes important and shows a fast increase with neutron energy. Note that the transportation process happens when a high-energy neutron enters the water phantom and goes out without performing any interaction.

In parallel, as we observe in Fig. 4.17, the secondary protons dominate the generated particles from a monoenergetic neutron beam in a water phantom. The number of these generated particles shows close values to the initial number of incident neutrons over the whole neutron energy range. In addition, this number decreases slowly when the incident neutron energy increases.

The generation of oxygen species in the water phantom seems to be very important as shown in Fig. 4.17. Oxygen 16 radicals dominate other oxygen species and their generation shows a maximum value for a neutron energy of around 1 MeV. On the other hand, the generation of

oxygen 17 and oxygen 18 radicals shows maximum values for a neutron energy of around 10 MeV.

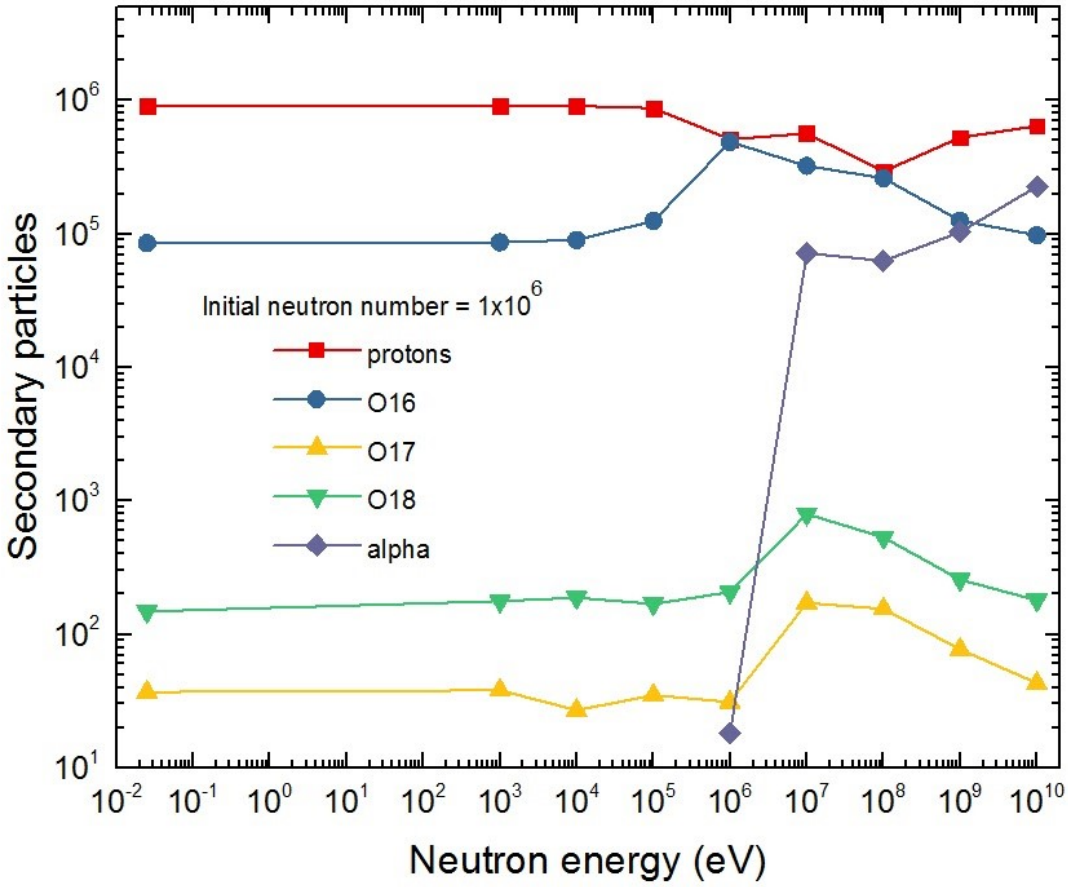

Figure 4.17 Variation of the generated particle number in a water phantom as a function of the incident neutron beam energy. Note that the initial number of neutrons in the incident beam interacting with the water phantom is set to 1×10^6.

The generation of secondary alpha particles neutrons in a water phantom starts to appear for a neutron energy of 1 MeV. It shows a fast increase with the neutron energy between 1 and 10 MeV while it increases slowly with a neutron energy above 10 MeV.

4.4.2: Correlation with neutron weighting factor

As shown in Fig. 4.17, the generation of secondary oxygen 16 radicals from the interaction of a monoenergetic neutron beam with a water phantom shows a maximum around a neutron energy of 1 MeV. This leads us to compare the energy dependence of secondary oxygen 16 generation and of the weighting factor of neutrons since the latter shows also a maximum around a neutron energy of 1 MeV as suggested by the ICRP 103 report.

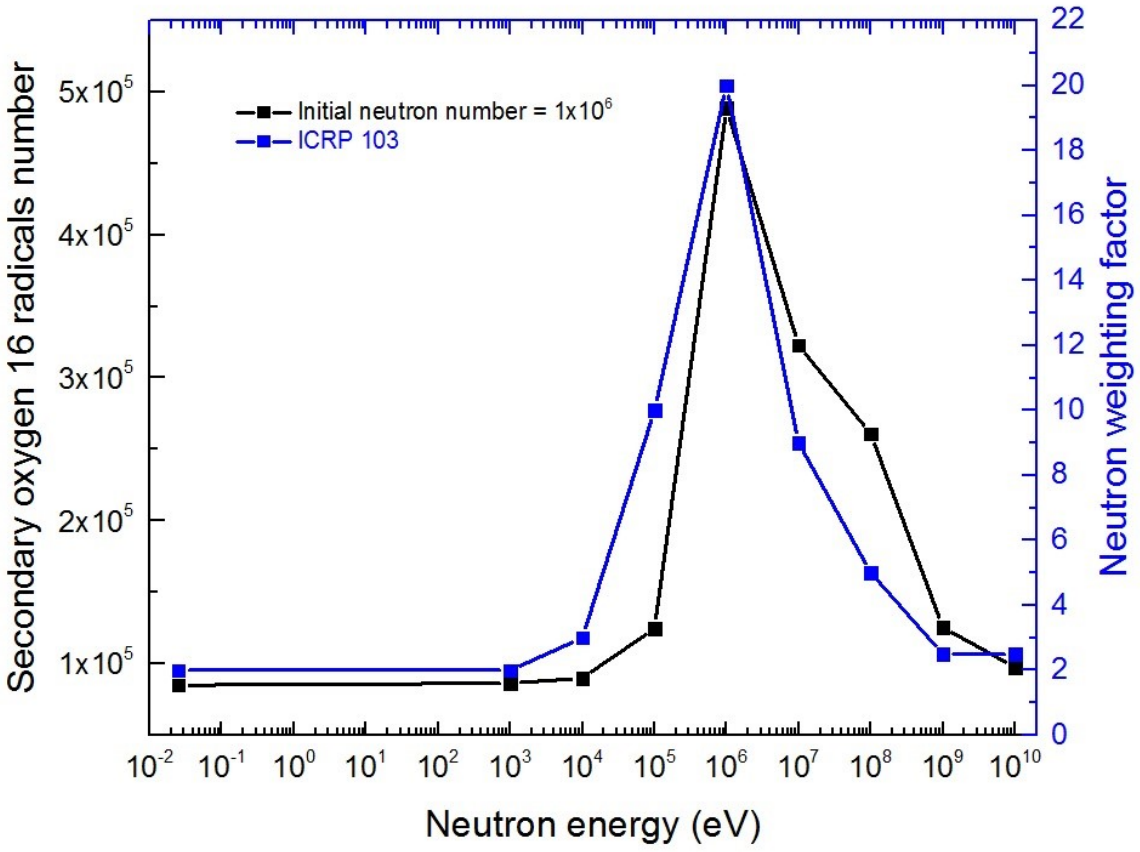

Figure 4.18 Energy dependence of neutron weighting factor as suggested by the ICRP 103 report and of the generation of secondary oxygen 16 radicals from the interaction of a monoenergetic neutron beam and a water phantom.

Fig. 4.18 shows a strong correlation between the variation of oxygen 16 generation and the variation of neutron weighting factor as a function of neutron energy. This correlation suggests a direct link between the biological effectiveness of neutrons and their ability to generate secondary oxygen radicals. As it is well known, oxygen radicals can cause huge damage to the cell DNA and a high amount of their generation can lead to an increase in the biological damage of cells.

Chapter 5: Conclusion and future work

Neutrons that are generated as secondary, byproduct, radiation during high-energy (>10 MeV) beam radiotherapy, cannot be shielded and consequently exposed patients are susceptible to radiocarcinogenesis. The carcinogenic risk is well known and generally accepted, although poorly understood. This project is motivated by the need to better understand dose deposition by secondary neutrons in radiotherapy so that their biological effects can be mitigated.

Two unfolding methods (MLEM and MAP) are used and compared with each other to ensure that we obtain accurate secondary neutron spectra and to evaluate precisely the risk related to these secondary neutrons in external beam radiotherapy (electrons and protons). At lower numbers of iterations, both methods give a similar evaluation of the secondary neutron spectra. At higher numbers of iterations, MLEM and MAP methods give different values above a certain number of performed iterations.

The neutron energy spectra were measured for electron (12 – 16 – 20 MeV) and proton (60 – 200 MeV) beams in various conditions and positions in the treatment rooms using a Nested Neutron Spectrometer. The raw measured data was unfolded using the MAP method.

The fluence rate of the secondary neutrons generated around an electron beam consists of a peak around an energy of 1 MeV due to evaporation processes, and a thermal peak due to neutrons that have scattered around the room and arrived at the measurement location. Neutrons also exist between these two peaks in the form of an intermediate energy continuum. The ambient dose equivalent rate of the secondary neutrons increases when increasing the electron beam energy and is higher when the jaws are closed indicating that an important generation of secondary neutrons around clinical electron beams does happen in the linac treatment head specially in the

collimation system. In parallel, the ambient dose equivalent rate of the secondary neutrons is similar with and without the presence of a solid water phantom along the electron beam path. This clearly indicates that the generation of secondary neutrons around clinical electron beams is not favorable in the phantom i.e. in the human body compared to linac head. In addition, the ambient dose equivalent rate decreases when the distance between the treatment beam and the measurement increases. This is due to the attenuation and absorption of the secondary neutrons generated around an electron beam as they travel in the treatment room.

The secondary neutrons generated around a proton beam in the treatment room have a wide energy range, from thermal up to the maximum beam energy which is equal to 200 MeV. This secondary neutron spectrum has three pronounced peaks. The first peak comprises direct neutrons and lies around 200 MeV. The second peak is due to evaporation processes and ranges from approximately 100 keV to approximately 10 MeV. The third is a thermal peak due to neutrons that have scattered around the room and arrived at the measurement location. Neutrons also exist between these peaks in the form of an intermediate energy continuum. The ambient dose equivalent rate of the secondary neutrons increases significantly when increasing the proton beam energy and is higher with the presence of a water phantom in the path of the proton beam. This clearly indicates that an important generation of secondary neutrons from clinical proton beams does happen in the water phantom, which means a relatively high generation of secondary neutrons in the patient body for a scanning proton beam. In addition, the ambient dose equivalent rate of the secondary neutrons is higher on the treatment couch than in the maze-room junction, which is due to the attenuation and absorption of the secondary neutrons generated around a proton beam as they travel in the treatment room.

By using Monte Carlo simulations, specifically GEANT4, we aimed to study neutron interactions with biological tissues, for instance the human body by determining the secondary species generated by these neutrons and verifying the energy dependence of the neutron weighting factor provided by the International Commission on Radiological Protection (ICRP) reports. The main neutron interaction is elastic scattering followed by neutron capture. The secondary protons dominate the generated particles from the interaction of a monoenergetic neutron beam (0.025 eV to 100 GeV) in a water phantom. The correlation between the variation of oxygen 16 generation and the variation of neutron weighting factor as a function of neutron energy suggests a possible link between the biological effectiveness of neutrons and their ability to generate secondary oxygen radicals.

As possible future work, a selection of the experimental conditions that should provide distinctly different carcinogenic potentials can be done (e.g. source spectra with very different thermal and fast neutron components and/or points of interest that experience very different secondary particle populations). For such future experimental work, many investigations are required: 1) scoring DNA damage at points of interest using track structure simulations. 2) examining DNA damage by ionizing photons as a control. 3) Biological measurements of DNA damage using various biodosimetry assays.

REFERENCES

[1] National cancer institute website (2015, February 9), Retrieved from https://www.cancer.gov/about-cancer/understanding/what-is-cancer

[2] Health Physics lectures, Medical Physics unit, McGill University

[3] E. B. Podgorsak, "Radiation physics for medical physicists". Springer, 2010

[4] F. M. Khan, "The physics of radiation therapy". Lippincott Williams and Wilkins, 2003

[5] T. Saito, H. Ishikawa, K. Ohnishi, T. Aihara, M. Mizumoto, N. Fukumitsu, K. Sugawara, T. Okumura and H. Sakurai, "Proton beam therapy for locally advanced and unresectable (T4bN0M0) squamous cell carcinoma of the ethmoid sinus: A report of seven cases and a literature review", Oncology Letters 10: 201-205, 2015

[6] D. Schardt, T. Elsässer and D. Schulz-Ertner, "Heavy-ion tumor therapy: Physical and radiobiological benefits", Rev. Mod. Phys., Vol. 82, No. 1, January–March 2010

[7] ICRP, "The 2007 Recommendations of the International Commission on Radiological Protection," tech. rep., ICRP, 2007

[8] J. Dubeau, S. S. Hakmana Witharana, J. Atanackovic, A. Yonkeu and J. P. Archambault, "A neutron spectrometer using nested moderators", Radiation Protection Dosimetry, Vol. 150, No. 2: 217– 222, 2012

[9] Nuclear power website (2016, March), Retrieved from http://www.nuclearpower.net/nuclear-power/reactor-physics/atomic-nuclear-physics/fundamental-particles/neutron/neutron-energy/

[10] G. F. Knoll, "Radiation detection and measurement". John Wiley and Sons, 2000

[11] Centronic website (2016, March), Retrieved from http://www.centronic.co.uk/products/8/boron-trifluoride-bf3-neutron-proportional-counters

[12] R. M. Maglieri, “A study of photoneutron spectra around high-energy medical linear accelerators using Monte Carlo simulations and measurements”, Master's thesis, 2014

[13] R. L. Bramblett, R. I. Ewing, and T. Bonner, “A new type of neutron spectrometer”, Nuclear Instruments and Methods, vol. 9, no. 1:1–12, 1960

[14] J. A. Cruzate, J. L. Carelli and B. N. Gregori, “Bonner sphere spectrometer”, Workshop on Uncertainty Assessment in Computational Dosimetry: A Comparison of Approaches. Bologna, Italy, 8-10 October 2007

[15] Bubble technology industries (2016, March), Retrieved from http://bubbletech.ca/product/bdt/

[16] E. B. Podgorsak, “Review of Radiation Oncology Physics: A Handbook for Teachers and Students”, International Atomic Energy Agency, Vienna, Austria, May 2003

[17] R. M. Howell and E. A. Burgett, “Secondary neutron spectrum from 250-MeV passively scattered proton therapy: Measurement with an extended-range Bonner sphere system”, Med. Phys. 41 (9), September 2014

[18] H. R. Vega-Carrillo and L. H. Pérez-Landeros, “Electroneutrons around 12 MeV linac”, Proceeding to the ISSD, 2012

[19] J. C. Liu, T. M. Jenkins, R. C. McCall, and N. E. Ipe, “Neutron dosimetry at Slac: Neutron sources and instrumentation”, SLAC-TN-91-3 October 1991

[20] R. Maglieri, A. Licea, M. Evans, J. Seuntjens, and J. Kildea, “Measuring neutron spectra in radiotherapy using the nested neutron spectrometer”, Medical Physics 42, 6162, 2015

[21] M. A. Haidekker, “Medical imaging technology”. Springer, 2013

[22] International Commission on Radiological Protection, “Conversion coefficients for use in radiological protection against external radiation,” Tech. Rep. ICRP Publication 74, International Organization for Standardization, 1996

[23] S. Agostinelli et al. “Geant4—a simulation toolkit”, Nuclear Instruments and Methods in Physics Research Section A: Accelerators, Spectrometers, Detectors and Associated Equipment Volume 506, Issue 3: 250-303, 2003